Earth System
Science
Data
Open Access
Discussions

1 **PMF-LP: the first 10 m plastic-mulched farmland distribution map (2019-2021) in**

2 **the Loess Plateau of China generated using training sample generation and**

3 **classifier transfer method**

4 Cheng Zhao [1, 2], Yadong Luo [1, 2], Xiangyu Chen [1, 2], Linsen Wu [1, 2], Zhao Wang [3], Hao Feng [2, 4],

5 Qiang Yu [3, 4], Jianqiang He [1, 2, 3, *]

6

7 [1] Key Laboratory for Agricultural Soil and Water Engineering in Arid Area of Ministry of Education, Northwest A&F

8 University, Yangling 712100, China

9 [2] Institute of Water-Saving Agriculture in Arid Areas of China, Northwest A&F University, Yangling 712100, Shaanxi,

10 China

11 [3] Key Laboratory of Eco-Environment and Meteorology for the Qinling Mountains and Loess Plateau, Shaanxi Provincial

12 Meteorology Bureau, Xi'an 710015, Shaanxi, China

13 [4] State Key Laboratory of Soil Erosion and Dryland Farming on the Loess Plateau, Institute of Water and Soil Conservation,

14 Northwest A&F University, Yangling 712100, Shaanxi, China

15

16 * *Correspondence to*: Jianqiang He (jianqiang_he@nwsuaf.edu.cn)

Abstract. Plastic film mulching has been extensively used to increase crop yields in arid and semi-arid regions, but it also altered agricultural landscapes and caused severe environmental pollution. Therefore, accurate and timely mapping of plastic-mulched farmland (PMF) distributions is crucial for planning agricultural production and preventing micro-plastic pollution. However, the scarcity of sufficient and representative training samples hinders large-scale supervised classification and extraction of PMF. Additionally, it remains unclear whether a pre-trained classifier can be directly applied to different regions and years for rapid PMF mapping. To address these challenges, we proposed a new framework that simultaneously takes advantages of the automation of index-based method and the generalization ability of supervised classifier-based approach for PMF mapping. Based on the distinctive spectral responses induced by plastic film deployment events, two novel and robust PMF indices—the Max Blue Band-based Plastic-mulched Farmland Index (MBPMFI) and the Blue Band-based Plastic-mulched Farmland Index (BPMFI)—were initially designed to automatically and rapidly extract PMF pixels in cloud-free areas as candidate training samples. Additionally, the transferability of classifiers pre-trained with these automatically generated samples and optimal features was further evaluated in spatial and spatial–temporal transferability scenarios using F1 values. Finally, by coupling the index-based training sample generation method with the temporal classifier transfer approach, PMF distributions were rapidly produced for the Loess Plateau of China (PMF-LP) for 2019–2021. The results showed that the two newly established indices, MBPMFI and BPMFI, were more robust than the existing PMF indices in enhancing PMF information and suppressing complicated backgrounds. The temporal classifier transfer proved suitable for directly and rapidly mapping PMF across multiple years without additional training samples. Using the locally adaptive classifiers as a reference, the average accuracy decrease of the transferred classifiers was less than 7.0% under the temporal transferability scenario. Our mapping framework achieved F1 values of 0.80–0.86 in recognizing PMF distributions for the Loess Plateau, highlighting its ability to delineate large-scale spatial patterns of PMF. Additionally, the estimated PMF areas based on the PMF-LP aligned well with the agricultural census data at municipal level ($R^2 > 0.87$). The framework developed in this study lays a foundation for future monitoring of PMF distributions and agricultural micro-plastic pollution on a large scale. The full archive of PMF-LP is freely available at https://doi.org/10.5281/zenodo.13369426 (Zhao et al., 2024).

1   Introduction

Plastic film mulching has been widely promoted and applied in China since 1978, due to its ability to improve grain crop yields and water use efficiency through conserving water, maintaining soil moisture, and increasing soil temperature (Liu et al., 2014; Sun et al., 2020; Zhao et al., 2023). Over the past 20 years, China has consistently ranked first in the world in terms of the usage and area of plastic film (Yang et al., 2015; Yan et al., 2014). The areas of plastic film mulching in China have increased from 11.0 million ha in 2000 to 17.6 million ha in 2020 (Zhang et al., 2022d). However, the extensive application of plastic films has also caused severe environmental issues. Plastic films, mainly composed of polyvinyl chloride, always have residues that are highly difficult to degrade in the soil, leading to severe "white pollution" (Liu et al., 2014; Kumar et al., 2020; Gao et al., 2019). Furthermore, plastic film mulching might have impacts on the regional climates, since the high-reflectivity and gas-tightness of the plastic film can alter the material and energy exchange between the land surface and the atmosphere (Lu et al., 2014; Zhao et al., 2023). Therefore, precise information about the spatial distributions of plastic-mulched farmland (PMF) over large areas is essential for planning agriculture production, mitigating plastic residue pollution, and understanding water and energy cycles in the agroecosystems (Veettil et al., 2023; Kumar et al., 2020).

Plastic film mulching data are usually derived from labor-intensive and time-consuming field surveys, and then documented by the statistical yearbooks. However, statistical data often lack accurate information about the locations and distributions of PMF. Benefiting from advances in Earth observation techniques, the quantity and accessibility of remote sensing images have increased, enabling effective large-scale monitoring of agriculture in a cost-effective and timely manner. (Maselli et al., 2020; Weiss et al., 2020; Phiri et al., 2020). In particular, Sentinel-2 satellites launched by the European Space Agency (ESA), provide data with a 10-m spatial resolution and a five-day revisit cycle, facilitating accurate monitoring of the Earth's surface (Drusch et al., 2012; Chaves et al., 2020). Furthermore, the emergence of cloud-based geospatial processing platforms, particularly the Google Earth Engine (GEE) (Gorelick et al., 2017), has significantly enhanced the processing capabilities of remote sensing data (Tamiminia et al., 2020; Pham-Duc et al., 2023). These advancements have supported the establishment of region- and nation-wide land cover maps, such as the China Land Cover Dataset (CLCD) (Yang and Huang, 2021) for China, and the Annual Crop Inventory (ACI) for Canada (Fisette et al., 2013). However, up to date, PMF has received comparatively less attention than crops, and regional or national PMF maps are rarely publicly available, particularly in China, where has the largest usage and area of plastic film.

Most optical satellite-based PMF mapping methods rely on spectral characteristics, as PMF can be easily differentiated from other land cover types during the crop sowing period (Hasituya et al., 2016; Xiong et al., 2019; Zheng et al., 2022). In this period, plastic films are applied to the surface of cultivated lands, resulting in a distinctive bright-white color characteristic for PMF (Lu et al., 2014; Hasituya et al., 2020). Thus, several studies have attempted to mapping PMF based on the unique color and spectral changes

80   caused by temporal variations in the "plastic film–vegetation–soil" composition (Lu et al., 2015; Xiong et

81   al., 2019; Hao et al., 2019; Fu et al., 2022; Zhou et al., 2023). Additionally, spectral indices derived from

82   images taken during the crop sowing period, such as the Plastic-mulched Landcover Index (PMLI) (Lu et

83   al., 2014) and the Modified Plastic-mulched Cropland Index (mPMCI) (Fu et al., 2022), have been used to

84   recognize PMF. Unfortunately, the time window for PMF recognition is very short (approximately one

85   month) and mainly spans from April to May in northern China (Xiong et al., 2019; Cheng et al., 2023). As

86   a result, obtaining seamless optical images over large areas during this period for index-based PMF

87   mapping is challenging due to the inevitable cloud contamination.

88   Another approach for PMF mapping is machine learning, which exhibits less dependence on images

89   obtained during the crop sowing periods. Owing to the predictive abilities of machine learning, even if a

90   PMF pixel is cloud-contaminated during the crop sowing period, machine learning classifiers can still

91   effectively identify it based on clear-sky images from other times (Zhang et al., 2022c; Wang et al., 2019;

92   Gao et al., 2023). Thus, machine learning classifiers such as the Random Forest (RF) and Support Vector

93   Machine (SVM) have been widely used for PMF mapping and achieved satisfactory accuracy (Hasituya

94   and Chen, 2017; Lu et al., 2018; Zheng et al., 2022). Additionally, the predictive capabilities of machine

95   learning classifiers combined with multi-temporal satellite observations also facilitated the seamless land

96   cover mapping at regional and national scales (Zhang et al., 2022c; Zhang et al., 2021a; Liu and Zhang,

97   2023). However, implementing machine learning classifiers for large-scale land cover classification,

98   particularly for PMF, remains a significant challenge due to the lack of abundant and representative training

99   samples (Skakun et al., 2017; Foody and Arora, 1997; Wen et al., 2022).

100   To train machine learning classifiers, it is an efficient method to leverage existing land use/cover maps

101   to obtain abundant training samples (Zhang et al., 2022b; Xuan et al., 2023; Zhang et al., 2022a; Zhang and

102   Roy, 2017). Unfortunately, there are no publicly available PMF maps in China, which limits the application

103   of this method. Since the index-based methods can rapidly and automatically identify specific land cover

104   types in areas with high-quality image observations (Deng and Wu, 2012; Zhang et al., 2022c), some

105   researchers have attempted to generate training samples for certain land cover types using index-based

106   methods to address the lack of base maps for training sample generation. Thus, index-based approaches,

107   combined with machine learning classifiers, have been gradually employed for automatic and seamless land

108   cover classification (Zang et al., 2023; Zhang et al., 2022c; Yang et al., 2023). For example, Zhang et al.

109   (2022c) demonstrated that integrating Winter Rapeseed Index-derived training samples with the RF

110   classifier can seamlessly and automatically recognize rapeseed in large cloudy regions. For PMF

111   recognition, most existing PMF indices were established in specific regions in Xinjiang Province, China

112   (Lu et al., 2014; Xiong et al., 2019; Hao et al., 2019; Fu et al., 2022). However, different from the large and

113   uniformly structured land parcels in Xinjiang, most regions in China typically have smaller and more

114   scattered land parcels. Thus, the existing PMF indices struggle to distinguish PMF from the complex and

115   fragmented backgrounds in these areas. Therefore, to fully leverage the strengths of index-based methods

116 and machine learning classifiers for automatic and seamless PMF mapping, a more robust PMF index is

117 urgently needed to separate PMF from other land cover types under diverse background conditions.

118   Moreover, classifier transfer, which involves applying classifiers trained in a source domain to

119 accomplish related tasks in a target domain, is also employed to address the scarcity of training samples

120 (Pan and Yang, 2009; Ma et al., 2024). This approach supports more rapid land cover mapping across large

121 scales and multiple years compare to locally adaptive classifiers. Consequently, it has been employed to

122 swiftly identify crop distributions in regions lacking ground reference samples and to retrace the spatial

123 distributions of historical crop types in the same region (Wang et al., 2019; Hu et al., 2022; Orynbaikyzy et

124 al., 2022; Qadir et al., 2024b; Qadir et al., 2024a). However, existing studies predominantly focused on

125 transferring supervised classifiers for crop classification. It remains unclear whether this approach is

126 applicable for the rapid mapping of PMF at large scales. And the factors influencing the accuracy of PMF

127 identification using this method are also unknown.

128   This study aimed to propose a novel framework for the rapid and automatic mapping of PMF

129 distributions across different regions and years at regional scales. Subsequently, we applied this framework

130 to mapping PMF distributions in the Loess Plateau of China from 2019 to 2021. The main objectives were:

131 (1) to automatically generate training samples based on newly proposed PMF indices that can robustly

132 enhance PMF information and suppress background noise under different background conditions; (2) to

133 assess the spatial–temporal transferability of the pre-trained classifiers for PMF mapping and identify the

134 factors that influence the transferability; (3) to rapidly and automatically produce seamless PMF

135 distribution maps (PMF-LP) for the Loess Plateau of China from 2019 to 2021 using the automatically

136 generated training samples and classifier transfer methods; and (4) to validate the accuracy of the PMF-LP

137 with independent ground samples and survey statistics.

138 **2 Study area and data**

139 **2.1 Study area**

140   This study identified PMF distributions from 2019 to 2021 in the Loess Plateau (33°43′ N–41°16′ N,

141 100°54′ E–114°33′ E) of China. The Loess Plateau covers an area of approximately 6.4×10^5 km², spanning

142 seven provinces: Qinghai, Gansu, Ningxia, Inner Mongolia, Shaanxi, Shanxi, and Henan (Fig. 1 (a)). This

143 region features diverse topography, with elevations ranging from about 300 meters above sea level in the

144 Guanzhong Plain to 5,000 meters in Qinghai Province (Fig. 1 (b)). According to the Köppen-Geiger climate

145 classification (Beck et al., 2023), the Loess Plateau experiences a warm temperate continental monsoon

146 climate, characterized by hot-rainy summers, and cold-dry winters (Fig. 1 (c)). The mean annual

147 precipitation varies across the region, from 200 mm in the northwest to 800 mm in the southeast, with 60–

148 70% of the total precipitation falling between July and October. The annual evapotranspiration ranges from

149 1,400 to 2,000 mm, and the average annual temperature varies between 3.6℃ and 14.3℃ (Li et al., 2024;

150 Tang et al., 2018; Li et al., 2012). Plastic-film mulching, an effective field management practice for storing

151 and maintaining soil moisture, is widely used across the Loess Plateau (Fig. 1 (d)~(g)) (Zhang et al., 2022f;
152 Wang et al., 2023). Notably, transparent plastic film predominates in this region, covering about 90% of the
153 total plastic-mulched fields (Lu et al., 2014; Wang et al., 2016; Hasituya et al., 2020). Thus, this study
154 focused solely on farmland mulched with transparent plastic film. To balance the computational cost and
155 the need for adequate training samples, the study area was divided into 32 mapping units based on the
156 municipal administrative boundaries (Fig. S1).

157 Three major crops—maize, potato, and winter wheat—are extensively cultivated in the Loess Plateau.
158 Maize and potato, the primary plastic-mulched crops, are typically sown in mid-April and harvested in late
159 September, with plastic film applied in a short time before and after sowing. Winter wheat is sown in
160 October of the prior year and harvested in late June. Only a very small portion of winter wheat is mulched
161 with plastic film in the study area. The crop calendars for these main crops were illustrated in Table 1.
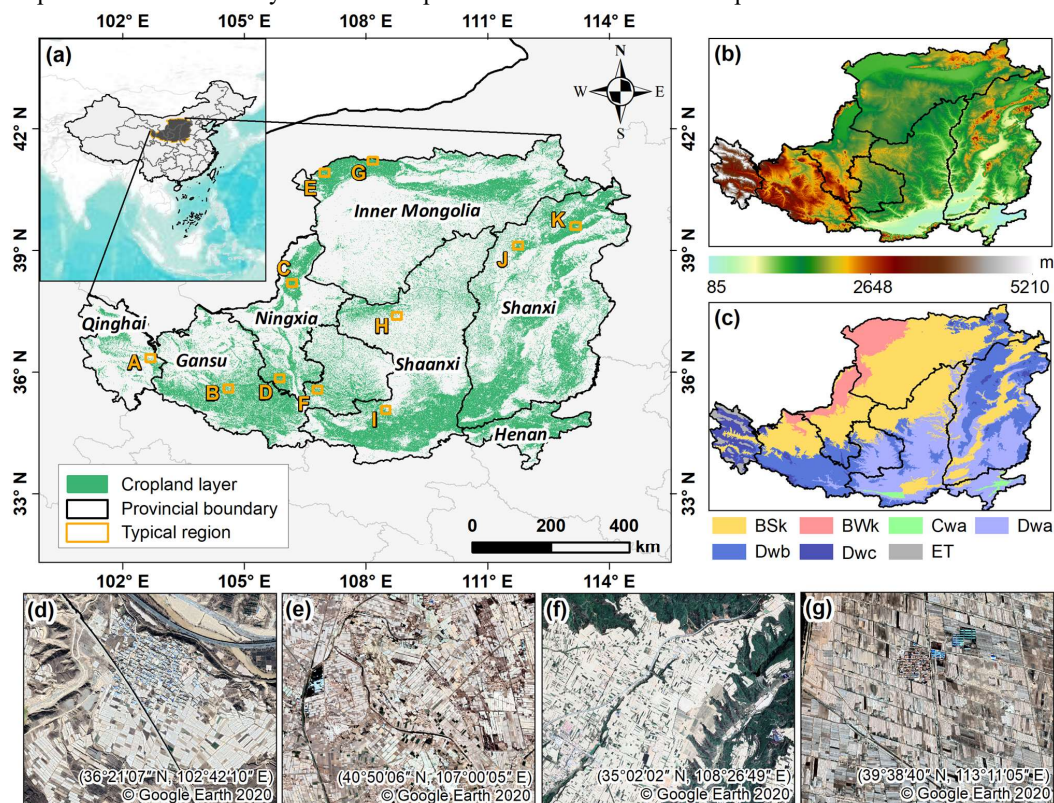
162

163 **Figure 1.** Overview of the study area. (a) Location of the Loess Plateau in China, spatial distributions of croplands.
164 Rectangular regions (A~K) are representative mulched regions where high-resolution Google Earth images are available
165 for visual intepretation. (b) Topography across the Loess Plateau. Digital Elevation Model (DEM) with a spatial resolution
166 of 30 m was obtained from the Shuttle Radar Topography Mission (SRTM) (Farr et al., 2007). (c) Köppen-Geiger climate
167 classification in the Loess Plateau. BSk: arid, steppe, cold; BWk: arid, desert, cold; Cwa: temperate, dry winter, hot summer;
168 Dwa: cold, dry winter, hot summer; Dwb: cold, dry winter, warm summer; Dwc: cold, dry winter, cold summer; and ET:
169 polar, tundra. (d)~(g) Zoom-in views of Google Earth images of plastic-mulched farmland during the mulching stage in
170 2020 for the rectangular regions of A, E, I, and K, reseptively.

171 **Table 1.**

172 Crop calendars illustrating growing phases of three major crops (i.e., maize, potato, and wheat) in the Loess Plateau of

173 China. The labels "E", "M", and "L" denote the early, middle, and last 10-day phases of a month.

Crops	Month																																			
	Jan			Feb			Mar			Apr			May			Jun			Jul			Aug			Sep			Oct			Nov			Dec		
	E	M	L	E	M	L	E	M	L	E	M	L	E	M	L	E	M	L	E	M	L	E	M	L	E	M	L	E	M	L	E	M	L	E	M	L
Maize										Sowing			Seeding			Jointing			Heading			Milk-ripe			Maturity											
Potato										Sowing			Seeding						Flowing			Tuber-swelling			Maturity											
Wheat	Seeding						Jointing			Earing			Maturity															Sowing			Seeding					

174

2.2 Data

2.2.1 Sentinel-2 data

177   The Sentinel-2 satellite, equipped with multispectral instruments, has 13 spectral bands covering

178 visible (10 m/pixel), near-infrared (20 m/pixel), and shortwave-infrared (20 m/pixel) wavelengths (Han et

179 al., 2021; Drusch et al., 2012). Its 5-day revisit cycle at the equator provides high-frequency Earth

180 observation data for monitoring rapid changes on the Earth's surface (Zhang et al., 2020b). In this study,

181 all available Sentinel-2 surface reflectance (SR) data covering the Loess Plateau from 2019 to 2021,

182 archived in GEE, were employed as input data since SR data are unavailable for this region before 2019.

183 The Sentinel-2 SR products in GEE platform have been pre-processed with radiometric and atmospheric

184 corrections. Considering the growth patterns of plastic-mulched crops (Table 1), Sentinel-2 data were

185 further limited to March to October, and quality assessment (QA) bands were used to mask clouds and

186 cirrus pixels.

187   Given that at least five points were required to fit a second-order harmonic regression curve whose

188 coefficients served as the input variables for the classifiers (Section 3.2), at least five images per pixel were

189 needed. We counted the number of yearly cloud-free images per pixel from 2019 to 2021 (Fig. S2), and

190 found that nearly 100% of the pixels in the study area had more than five observations each year. The mean

191 numbers of cloud-free images per pixel were 46 in 2019, 45 in 2020, and 43 in 2021, respectively. Therefore,

192 the Sentinel-2 time series images provided ample data for the image processing requirements of this study.

2.2.2 Cropland mask

194   To simplify the process of PMF mapping and reduce commission errors caused by other land cover

195 types (Zhang et al., 2023; You et al., 2023; You et al., 2021; Defourny et al., 2019), two cropland layers,

196 including the ESA WorldCover 2020 (Zanaga et al., 2022) and the China Land Cover Dataset (CLCD)

197 (Yang and Huang, 2021) of 2020, were overlapped and utilized to exclude non-cropland pixels in this study.

198 The idea to incorporate two different cropland layers was driven by the assumption that relying on a single

199 cropland layer could introduce uncertainties, while combining two layers could generate cropland pixels

200 with a higher confidence level (You et al., 2023). Since the CLCD has a spatial resolution of 30 m, we re-

201 sampled it to a 10-m resolution using the nearest-neighbor method. Given the relatively stable nature of

202   cropland across adjacent years (Gong et al., 2019), we applied the overlapped cropland layer in 2020 to
203   mask Sentinel-2 images for each year from 2019 to 2021.

### 2.2.3 Google Earth high-resolution images (GE-HRIs)

205   Google Earth high-resolution images, sourced from the Google Earth platform, provide satellite and
206   aerial imagery of the Earth's surface with a sub-meter spatial resolution of 0.6 m, which facilitates sample
207   collection through visual interpretation. Therefore, the GE-HRIs were utilized to assist in obtaining
208   validation samples in this study. Additionally, two representative rectangular regions (20 km × 20 km) with
209   at least one GE-HRI image available during the mulching stage were selected in each province (yellow
210   areas A~K in Fig. 1(a)). The samples interpreted in these rectangular regions (300 PMF/Non-PMF points
211   for each region) were employed to determine optimal thresholds for the newly proposed PMF indices in
212   Section 3.1.2.

2.2.4 Agricultural statistics

214   The PMF census data from 2019 to 2021, sourced from municipal-level agricultural statistical offices,
215   were collected to assess the mapped PMF areas. It is noteworthy that plastic film usage in the statistical
216   yearbooks of most cities in the Loess Plateau is quantified in tons. Consequently, in this study, we only
217   obtained statistical data for 12 cities (Fig. S3), where plastic film usage was measured in terms of area.
218   Since these 12 cities account for nearly one-third of the total area of the Loess Plateau, the accuracy
219   assessment of the mapped PMF areas based on the municipal statistical data was considered representative
220   and reliable.

3   Methodology

222   The workflow of this study was summarized in Fig. 2. First, cloud-free Sentinel-2 time series data
223   were used to fit harmonic curves, generating feature variables that served as input variables for the
224   classifiers. Next, a temporal signature analysis of various cropland-related land covers was conducted.
225   Distinctive signatures during the mulching period guided the design of PMF indices, which effectively
226   separated PMF from other land cover types. These indices were then employed to identify PMF in cloud-
227   free areas and automatically generate training samples. Third, random forest classifiers were developed to
228   recognize PMF based on the feature variables and the automatically generated training samples. The
229   transferability of these classifiers was then evaluated in terms of temporal and spatial–temporal
230   transferability. Finally, the PMF mapping results were assessed against ground reference samples and
231   statistical PMF area data.
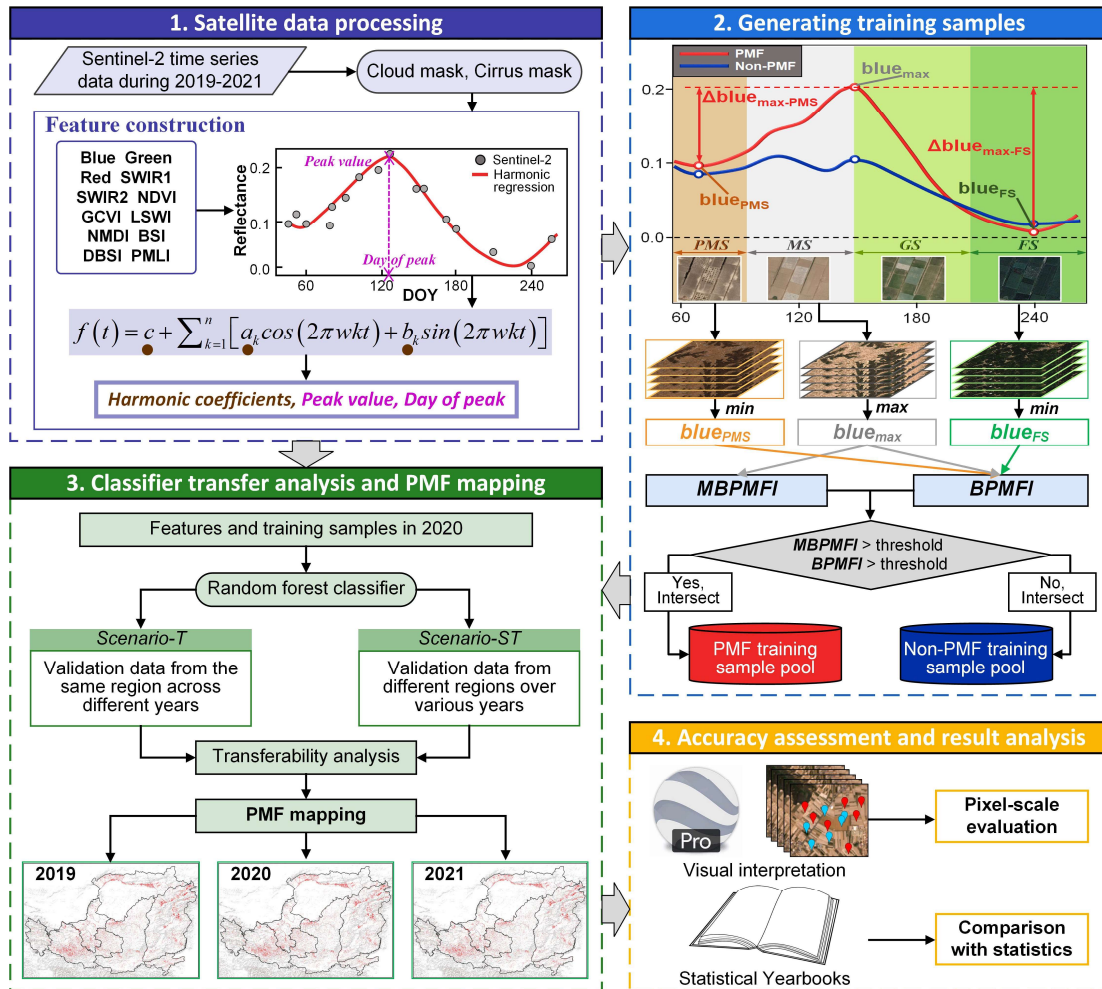
Figure 2.   Flowchart depicting the integration of index-based training sample generation and classifier transfer for plastic-mulched farmland mapping. PMF: Plastic-mulched Farmland, Non-PMF: Non-plastic-mulched Farmland. The entire growing season of plastic-mulched crops was divided into four stages: pre-mulching stage (PMS), mulching stage (MS), growing stage (GS), and flourishing stage (FS) (Section 3.1.2). The MBPMFI (Max Blue Band-based Plastic-mulched Farmland Index) and BPMFI (Blue Band-based Plastic-mulched Farmland Index) are the two novel PMF indices proposed in this study (Section 3.1.2).

3.1 Automatically generating training samples

3.1.1 Optical characteristics of the PMF

The multi-temporal Sentinel-2 images with true-color composites from a representative sub-region in Pingliang City, Gansu Province, were shown in Fig. 3 (c)~(j) to analyze the optical characteristics of PMF. The PMF, plastic greenhouses (PGs), and vegetation (mainly winter crop) within this sub-region represented the primary agricultural-related land cover types on the cultivated farmland in the Loess Plateau. During the crop sowing period, PMF exhibited a bright-white color due to the plastic films, making it easily

246   distinguishable from vegetation (dark-green color) but potentially confusing it with PGs (blue-gray or white
247   color) (Fig. 3 (c)~(f)). Subsequently, from June to September (Fig. 3 (g)~(i)), the crop canopy covered the
248   PMF, giving it a green appearance similar to vegetation. Meanwhile, since crops grew inside the PGs, the
249   PGs maintained blue-gray or white appearance consistently. Thus, this period was ideal for differentiating
250   between PGs and PMF.

251   Based on this analysis, we observed that PMF exhibited a bright-white appearance during the crop
252   sowing period. Theoretically, the conspicuous bright white characteristic indicated the substantial
253   reflectance of PMF in the visible spectrum. Temporal profiles of the Sentinel-2 blue band reveled
254   distinguishable patterns among PMF, PGs, and vegetation (Fig. 3 (b)). Specifically, during the crop sowing
255   period, areas covered by plastic films had higher reflectance in the blue band compared to those covered
256   by the crop canopy. Subsequently, as crops grew in the PMF, the increased absorption in the visible
257   spectrum led to a gradual decrease in PMF reflectance in the blue band. Particularly, during the peak
258   growing stage of crops, PMF reached its lowest reflectance in the blue band.

259   In addition to the blue band, PMF demonstrated clear differentiation from other land cover types in
260   the green and red bands, as well as in the red-edge band (red edge1) (Fig. S4). Notably, this study focused
261   exclusively on the blue band due to the consistent temporal profiles observed across these four bands.
262   Furthermore, the distinct PMF characteristics in the blue band were also tested across different regions in
263   the Loess Plateau (Fig. S5). The results showed that PMF reflectance in the blue band exhibited the same
264   temporal profiles as those illustrated in Fig. 3 (b), characterized by a rapid increase during the crop sowing
265   period, followed by a swift decrease during the flourishing period.
266
267
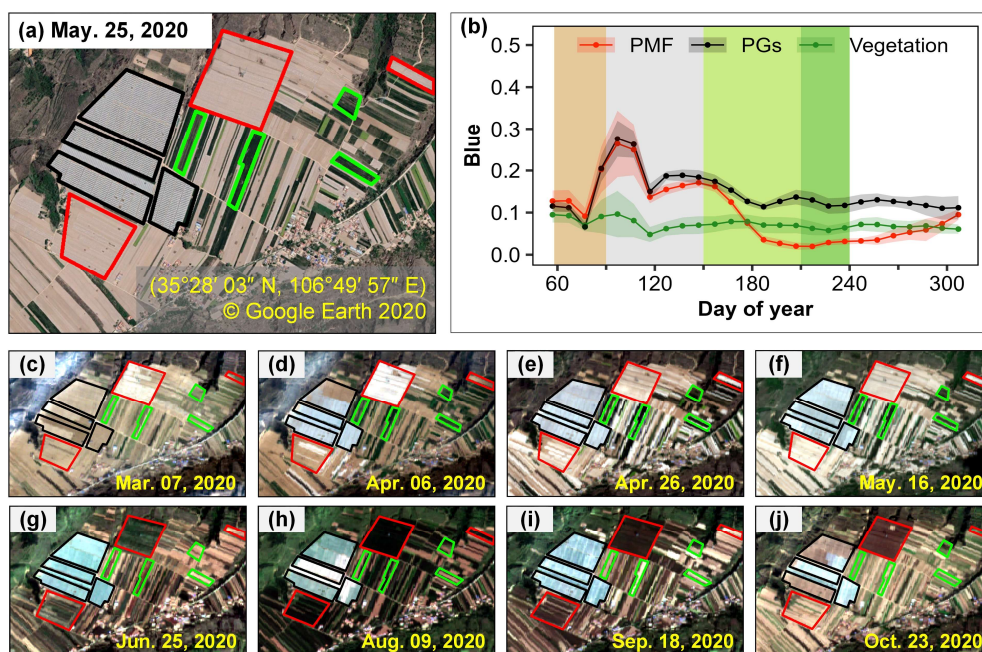
Figure 3. Time-series profiles of plastic-mulched farmland (PMF), plastic greenhouses (PGs), and vegetation in a representative sub-region of Pingliang City, Gansu Province, China. (a) High-resolution Google Earth imagery during the crop sowing period. The red, black, and green outlined plots denote the PMF, PGs, and vegetation, respectively. (b) Time series of PMF, PGs, and vegetation in the Sentinel-2 blue band. The red, gray, and blue buffers indicate one standard deviation. The brown, gray, yellowish-green, and green rectangular areas denote the pre-mulching stage (PMS), mulching stage (MS), growing stage (GS), and flourishing stage (FS) as defined in Section 3.1.2, respectively. (c)~(j) Sentinel-2 images with a true-color composite of blue, green, and red bands on different dates across the entire crop growing season.

3.1.2 Developing PMF indices to automatically generate training samples

Following the temporal profile analyses in Section 3.1.1, the entire growing season of plastic-mulched crops was divided into four distinct stages (Fig. 4). The pre-mulching stage (PMS) (March to early April) involves primarily field plowing, with seldom plastic film coverage on the farmland. The mulching stage (MS) (mid-April to May) represents the gradual coverage of farmland with plastic films. During the growing stage (GS) (June to July), crops begin to grow but do not yet fully cover the cropland. The flourishing stage (FS) (August to September) is characterized by vigorous crop growth, with the crop canopy fully sheltering the cropland.

Across these stages, the distinctive spectral responses of PMF in the blue band were summarized as follows: a relatively large range of reflectance dynamics from PMS to MS ($\Delta blue_{max-PMS}$) due to the gradual deployment of plastic film, and the maximal range of reflectance dynamics from GS to FS ($\Delta blue_{max-FS}$) due to the abundant visible spectrum absorption for photosynthesis. Considering that both $\Delta blue_{max-PMS}$ and $\Delta blue_{max-FS}$ for PMF were relatively higher than those for other land cover types, multiplying these two metrics could effectively highlight PMF while suppressing other land cover types. Specifically, two
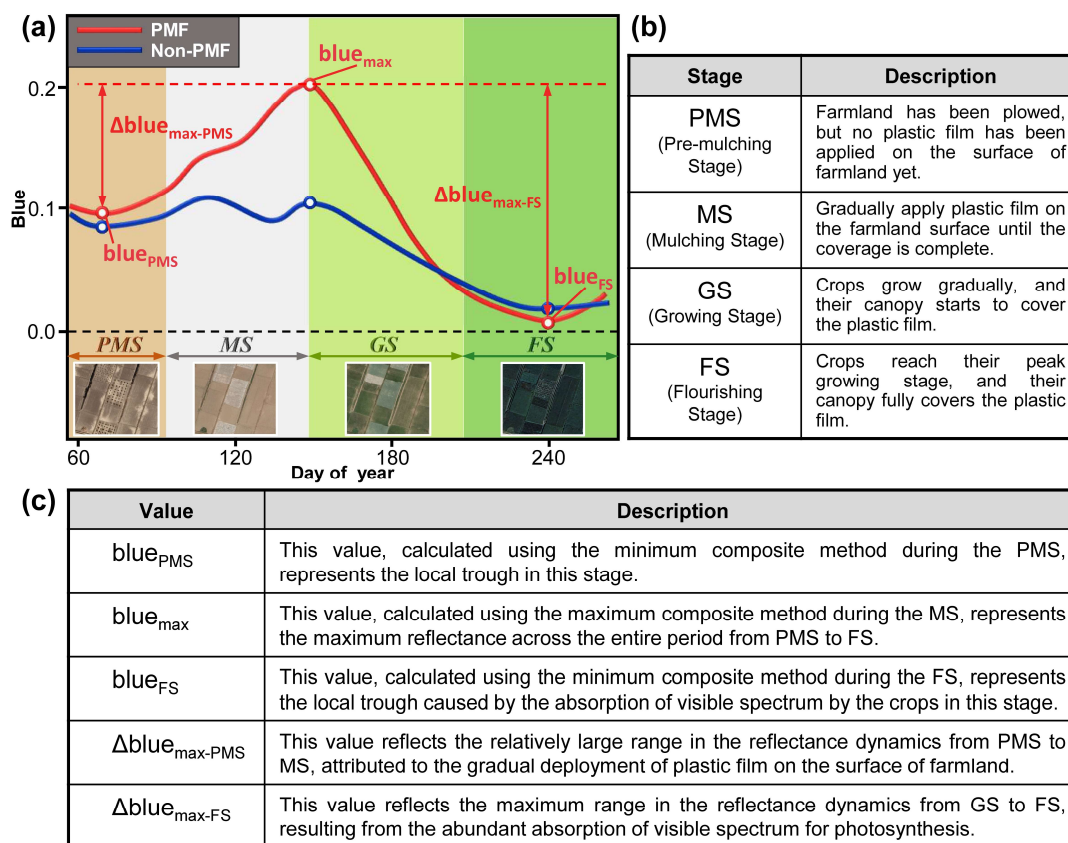
290   local troughs (blue$_{PMS}$ and blue$_{FS}$) are the minimum reflectance values of the blue band during the PMS and

291   FS, respectively. The local peak (blue$_{max}$) refers to the maximum reflectance value of the blue band during

292   the MS. Additionally, the metric blue$_{max}$ was also employed to enhance PMF signals, as it exhibited the

293   highest reflectance value throughout the period from PMS to FS. Finally, two PMF indices, the Max Blue

294   Band-based Plastic-mulched Farmland Index (MBPMFI) (Eq. (1)) and the Blue Band-based Plastic-

295   mulched Farmland Index (BPMFI) (Eq. (2)) were defined.

$$MBPMFI = blue_{max} \tag{1}$$

$$BPMFI = 100 \times \Delta blue_{max\text{-}PMS} \times \Delta blue_{max\text{-}FS} = 100 \times \left(blue_{max} - blue_{PMS} \right) \times \left(blue_{max} - blue_{FS} \right) \tag{2}$$

298   where the multiplier 100 was used to linearly stretch the BPMFI to a wider range.

Stage	Description
PMS (Pre-mulching Stage)	Farmland has been plowed, but no plastic film has been applied on the surface of farmland yet.
MS (Mulching Stage)	Gradually apply plastic film on the farmland surface until the coverage is complete.
GS (Growing Stage)	Crops grow gradually, and their canopy starts to cover the plastic film.
FS (Flourishing Stage)	Crops reach their peak growing stage, and their canopy fully covers the plastic film.

| Value	Description
blue$_{PMS}$	This value, calculated using the minimum composite method during the PMS, represents the local trough in this stage.
blue$_{max}$	This value, calculated using the maximum composite method during the MS, represents the maximum reflectance across the entire period from PMS to FS.
blue$_{FS}$	This value, calculated using the minimum composite method during the FS, represents the local trough caused by the absorption of visible spectrum by the crops in this stage.
Δblue$_{max\text{-}PMS}$	This value reflects the relatively large range in the reflectance dynamics from PMS to MS, attributed to the gradual deployment of plastic film on the surface of farmland.
Δblue$_{max\text{-}FS}$	This value reflects the maximum range in the reflectance dynamics from GS to FS, resulting from the abundant absorption of visible spectrum for photosynthesis.

Figure 4.   Schematic diagrams illustrating the construction of the plastic-mulched farmland indices. (a) Time-series profiles of the plastic-mulched farmland (PMF) and non-plastic-mulched farmland (Non-PMF) in the Sentinel-2 blue band. (b) Defined stages used to divide the entire growing season of plastic-mulched crops into four parts. (c) Explanation of the variables used to represent the unique characteristics of PMF.

305   Notably, since the primary objective of this study was to recognize PMF and given the relative scarcity

306   of PGs compared with PMF (Feng et al., 2021; Tong et al., 2024), land cover types were categorized into

307   two classes: PMF and Non-PMF. Table S1 presented the statistical analysis results of the MBPMFI and

308   BPMFI indices for both PMF and Non-PMF samples collected from the rectangular regions (Section 2.2.3).

309   Generally, the *p-values* for the two PMF indices across different provinces were equal to 0, indicating the

310   great potential of MBPMFI and BPMFI to enhance PMF signals while suppressing Non-PMF signals.

311   Referring to previous studies (Zhang et al., 2022g; Zhou et al., 2024), sample points from the rectangular

312   regions were exploited to establish province-specific thresholds for each PMF index. The optimal

313   thresholds for the two novel indices were separately determined based on accuracy information with

314   different thresholds (Fig. 5). Particularly, for Henan Province, we adopted the same thresholds as those used

315   in Shanxi Province. Finally, PMF and Non-PMF pixels in cloud-free areas were automatically extracted.

316   To improve the reliability of the training samples, only cropland classified as PMF or Non-PMF by both

317   PMF indices was included in the final training sample pools (Fig. 6).
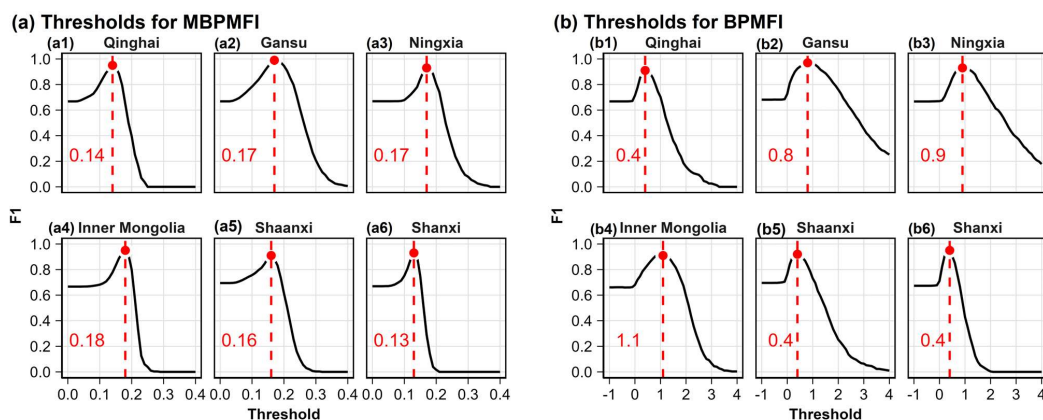
318
319   **Figure 5.**   Classification accuracy curves of various plastic-mulched farmland indices at different thresholds.
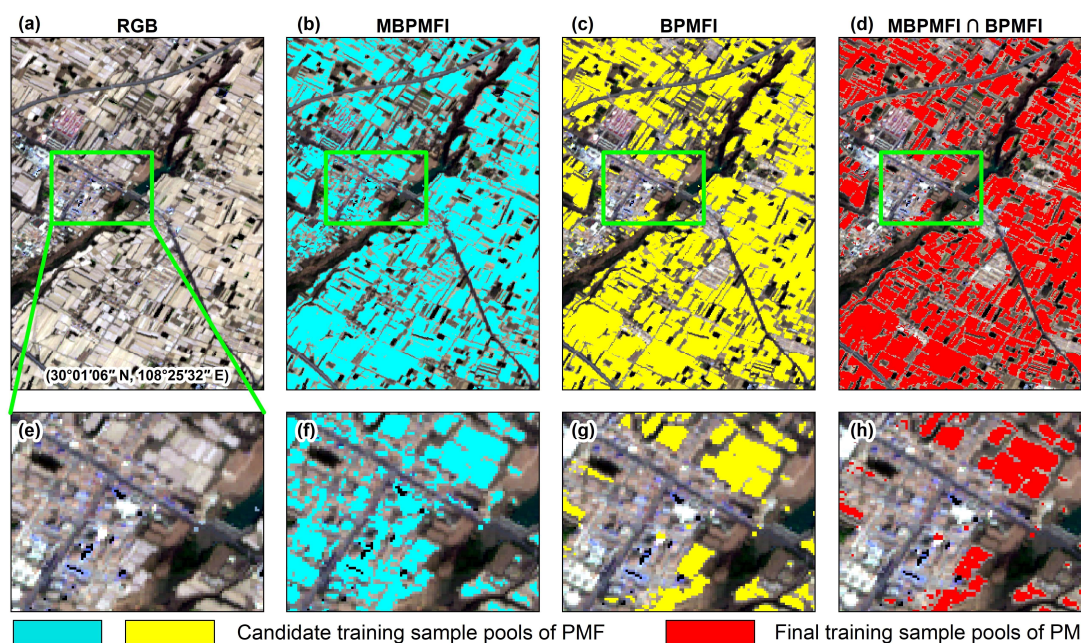
Figure 6. Zoomed-in views for illustrating the detailed process of training sample generation. (a) Sentinel-2 images with a true-color composite of blue, green, and red bands. (b) Candidate training sample pool derived based on MBPMFI (Max Blue Band-based Plastic-mulched Farmland Index). (c) Candidate training sample pool derived based on BPMFI (Blue Band-based Plastic-mulched Farmland Index). (d) Final training sample pool. "∩" means the intersection is implemented for sample pools of MBPMFI and BPMFI. (e)~(h) Zoomed-in views from the green frame in (a) for presenting the misclassification between plastic-mulched farmland (PMF) and impervious surfaces.

3.1.3 Training sample generation and refinement

Based on the candidate sample pools generated in Section 3.1.2, a stratified random sampling approach was adopted to select 2000 pixels for PMF and Non-PMF within every mapping unit for the year 2020. To further ensure the reliability of these samples and eliminate potential errors, a strict spatial filter (8-neighbor filter) was conducted for these samples (Zhang et al., 2022a; Zhang et al., 2023; Zhang and Roy, 2017). Only pixels sharing the same class type as the surrounding eight pixels were considered as high-quality samples. These samples were utilized as training data for subsequent classifiers to identify PMF.

3.2 Feature calculation and selection

The visible bands (Blue, Green, and Red) and shortwave-infrared bands (SWIR1 and SWIR2) from Sentinel-2 were selected as input features for classifiers, due to their high potential to separate PMF from other land cover types (Hasituya et al., 2016; Xiong et al., 2019; Hao et al., 2019). Since plastic films can influence energy balance and water cycles on the land surface (Lu et al., 2014; Hasituya and Chen, 2017), several remote-sensing vegetation indices associated with vegetation and soil conditions were also included as input features (Table S2): NDVI (Tucker, 1979), GCVI (Gitelson et al., 2005), LSWI (Xiao et al., 2002), NMDI (Wang and Qu, 2007), BSI (Rikimaru et al., 2002), DBSI (Rasul et al., 2018), PMLI (Lu et al., 2014).

342   Moreover, the newly proposed PMF indices, MBPMFI and PMFI, were also incorporated.

343   Compared with Non-PMF, PMF exhibited unique temporal profiles resembling sine waves in the blue

344   band (Fig. 4 (a), Fig. S5). To characterize these profiles and fill missing values caused by cloud

345   contaminations, harmonic regression (Jakubauskas et al., 2001; Zhou et al., 2022) (Eq. (3)) was conducted

346   to fit time series curves for PMF across the five surface reflectance bands and seven vegetation indices. The

347   time window for fitting the time-series curves extended from March 1st to October 31st, covering the entire

348   growing season of plastic-mulched crops. Each band was treated as a time-dependent function, denoted as

349   f(t).

$$f\left(t\right) = c + \sum_{k=1}^{n}\left[a_k \cos\left(2\pi k \omega t\right) + b_k \sin\left(2\pi k \omega t\right)\right] \tag{3}$$

351   where the independent variable t is the day of year expressed as a fraction between 0 (January 1st) and 1

352   (December 31st) for a satellite image, c is the intercept term, n is the order of harmonic series, a_k are the

353   cosine coefficients, b_k are the sine coefficients, and ω is the angular frequency.

354   In the above harmonic regression formula, parameters n and ω need to be adjusted to balance the fitting

355   closeness to the observation points and prevent overfitting. Based on the ground reference PMF samples

356   within the rectangular regions (yellow areas A~K in Fig. 1 (a)), we picked n = 2 and ω = 1.5 as the optimal

357   parameters by evaluating the root mean square error (RMSE) of the fitting progress (Fig. S6). Therefore,

358   we obtained the final harmonic regression formula (Eq. (4)).

$$f\left(t\right) = c + a_1 \cos\left(3\pi t\right) + b_1 \sin\left(3\pi t\right) + a_2 \cos\left(6\pi t\right) + b_2 \sin\left(6\pi t\right) \tag{4}$$

360   After the harmonic regression, the time series of each band was represented by five coefficients: c, a_1, b_1,

361   a_2, and b_2. Furthermore, the peak value (peak) of each band and their corresponding dates (timing) were

362   also extracted from the fitted harmonic regression curves. These coefficients combined with MBPMFI and

363   BPMFI resulted in a total of 86 (12 × 7 + 2 = 86) features.

364   To select the important features and discard unimportant ones which may adversely affected the

365   accuracy and computational cost of supervised classifiers (Zou et al., 2015; Wang et al., 2022b), a

366   combination of time-series correlation analysis and random forest feature importance analysis was

367   employed to reduce the number of features (Fig. S7). The reduction process included: (1) grouping bands

368   with correlation coefficients exceeding 0.90, retaining only the band with the highest feature importance

369   (retained bands: Blue, SWIR2, BSI, DBSI, GCVI, NMDI, and PMLI); (2) further limiting the seven

370   harmonic coefficients to the peak, a_1, and b_2 terms based on their importance evaluation results; (3) retaining

371   MBPMFI and BPMFI due to their higher importance compared with other features (Fig. 7). Ultimately, a

372   total of 23 features were adopted as input variables for the classifiers in this study. A comparison of PMF

373   identification accuracies using 86 features versus 23 features revealed no significant difference (α = 0.05)

374   in classification accuracy between the two sets of features (Fig. S8).
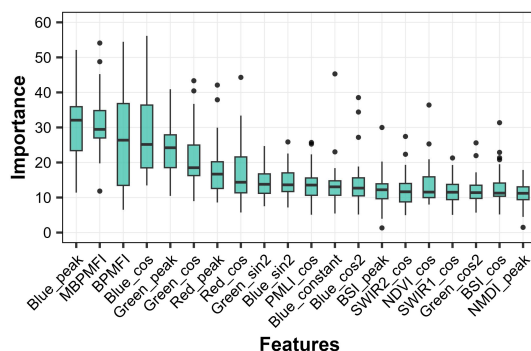
Figure 7. Feature importance of top 20 features calculated by the random forest classifiers trained in each city in the Loess Plateau. Since the feature importance in each city is not comparable, we normalized the individual value by dividing the total importance of all features in each city and scaled them by multiplying 1000.

3.3 Classifier transferability analysis

We employed the pixel-based random forest (RF) classifier (Breiman, 2001) available on the GEE platform to distinguish PMF from Non-PMF for each mapping unit, based on the selected optimal features and automatically generated samples mentioned above. As an ensemble algorithm comprising numerous decision trees, RF has been widely used for large-scale land cover classification (Zhang et al., 2021c; Liu et al., 2020), crop type mapping (Yang et al., 2023; Wang et al., 2020), and classifier transferability analysis (Wijesingha et al., 2024; Qadir et al., 2024b), due to its capabilities in handling high-dimensional data, tolerating noise, and preventing overfitting (Belgiu and Drăguţ, 2016; Sheykhmousa et al., 2020). Two key hyperparameters need to be set when using RF, which are the number of trees (*Ntree*) to be generated and the number of features(*Mtry*) used for testing the best split when growing the trees (Belgiu and Drăguţ, 2016). The former parameter was set as 100 since the out-of-bag errors in different mapping units ceased to decrease beyond 100 trees (Fig. S9); the latter one was set as the default value (i.e., the square root of the number of features).

Revealing the temporal and spatial–temporal transferability of classifiers can facilitate multi-year PMF mapping without the need to collect domain- and year-specific training samples. The classifiers trained with the optimal features and automatically generated samples in each mapping unit in 2020 (reference scenario, Scenario–Ref) were tested in two transferability scenarios to evaluate their temporal and spatial–temporal transferability: (1) classifiers trained in each mapping unit in 2020 were applied to recognize PMF within the same units for 2019 and 2021 to assess their temporal transferability (Scenario–T); and (2) classifiers trained in each mapping unit in 2020 were employed to recognize PMF in all other remaining units for 2019 and 2021 to test their spatial–temporal transferability (Scenario–ST). Note that classifiers trained with data from 2020 were not assessed in other spatial regions in the same year of 2020 because the primary goal of classifier transfer in this study is to rapidly retrace historical PMF distributions. Additionally, we trained classifiers in each mapping unit (municipal level) because sample point collection in practice is usually

403 conducted within administrative boundaries rather than in agro-ecological boundaries (Hao et al., 2020;

404 Wang et al., 2019). In each scenario, the F1-score (F1) was calculated based on validation samples as

405 accuracy evaluation metric. Furthermore, to assess changes of F1 in each transferability scenario against

406 reference scenario, a percentage change of F1 values (F1$_{change}$) was also computed (Eq. (5)).

407
$$F1_{change} = \frac{F1_{transferability} - F1_{reference}}{F1_{reference}} \times 100 \qquad (5)$$

408 **3.4 Accuracy assessment**

409 We assessed the quality of the generate PMF maps with two measures. First, we performed a pixel-

410 wise quantitative assessment for the PMF maps in 2019–2021, using more than 5000 ground reference

411 samples each year (Table S3). Four accuracy metrics were adopted: producer accuracy (PA), user accuracy

412 (UA), overall accuracy (OA), and F1-score (F1). Next, the coefficient of determination (R^2) was used to

413 quantitatively measure the consistency of the PMF areas derived from agricultural statistics and those from

414 the resultant maps. Due to the lack of publicly available PMF products in China, inter-comparison with

415 existing products was not possible in this study.

416 The validation samples were collected by visually interpreting GE-HRIs and Sentinel-2 images, based

417 on the unique characteristics of PMF (Section 3.1.1). A two-step strategy was designed to generate the

418 validation samples: (1) croplands exhibiting a white hue during the mulching stage (MS) and a dark green

419 hue during the flourishing stage (FS) in the true-color composite images were more likely to be PMF than

420 those showing other hue changes; (2) the time-series curves of PMF in the blue band displayed more

421 pronounced peak values during the mulching stage (MS) and trough values during the flourishing stage (FS)

422 compared to other land cover types. Pixels meeting above two rules were finally labeled as PMF; otherwise,

423 they were grouped into Non-PMF. Ultimately, we obtained 7,091, 12,140, and 6,714 validation samples for

424 2019, 2020, and 2021, respectively (Table S3, Fig. S10).

425 Moreover, five additional PMF indices (Table 2), including PMLI (Lu et al., 2014) (Eq. (6)), PMFI$_{first}$

426 (Xiong et al., 2019) (Eq. (7)), PMFI$_{second}$ (Xiong et al., 2019) (Eq. (8)), PMLI$_{SWIR}$ (Hao et al., 2019) (Eq.

427 (9)), and mPMCI (Fu et al., 2022) (Eq. (10)), were utilized to compare with the newly established MBPMFI

428 and BPMFI indices in enhancing PMF information while suppressing Non-PMF information. Except for

429 the PMLI, higher values of these indices are more related to PMF. To test the robustness of these indices,

430 three representative regions with diverse environmental conditions were selected: (1) Region I, located in

431 Bayan Nur City, Inner Mongolia Province, exhibits a large and densely distributed PMF area in this region

432 (Fig. 8 (a)); (2) Region II, located in Linxia City, Gansu Province, features an irregularly shaped PMF with

433 sparse distribution (Fig. 9 (a)); and (3) Region III is located in Xianyang City, Shaanxi Province, where

434 some plastic greenhouses and buildings exhibit similar spectral profiles to PMF (Fig. 10 (a)). A visual

435 evaluation was conducted to intuitively compare the performance of these indices. Since the presence of

436 noises in the index images could affect their display and subsequently influence the visual comparison

437 results, all index images were displayed with a 1% linear stretch (Zhang et al., 2022g) to ensure the fairness

438 of visual comparison among them.

439 **Table 2.**

440 Summary of the existing plastic-mulched farmland indices used for comparison with the newly established MBPMFI and

441 BPMFI indices in this study.

Name	Equation*	Equation index
PMLI (Plastic-mulched Landcover Index)	$\dfrac{\rho_{SWIR1} - \rho_{Red}}{\rho_{SWIR1} + \rho_{Red}}$	(6)
PMFI$_{first}$ (Plastic-mulched Farmland Index First)	$\dfrac{\rho_{SWIR2}}{\rho_{NIR}}$	(7)
PMFI$_{second}$ (Plastic-mulched Farmland Index Second)	$\dfrac{\rho_{SWIR2}}{\rho_{Blue}}$	(8)
PMLI$_{SWIR}$ (Plastic-mulched Land Index with Shortwave-infrared Band)	$\dfrac{(\rho_{RE4} + \rho_{NIR} + \rho_{RE3}) - (\rho_{SWIR1} + \rho_{SWIR2})}{\rho_{SWIR1} + \rho_{SWIR2}}$	(9)
mPMCI (Modified Plastic-mulched Cropland Index)	$\dfrac{\rho_{SWIR1} + \rho_{NIR}}{\rho_{SWIR1} - \rho_{NIR}}$	(10)

442 * ρ_{blue}, ρ_{red}, ρ_{nir}, ρ_{RE3}, ρ_{RE4}, ρ_{SWIR1}, and ρ_{SWIR2} represent the Sentinel-2 reflectance in the blue band (496 nm), red band

443 (665 nm), near-infrared band (833 nm), red-edge 3 band (779 mm), red-edge 4 band (864 mm), shortwave-infrared band

444 1 (1610 mm), and shortwave-infrared band 2 (2185 mm), respectively.

4 Results

### 4.1 Comparisons with existing PMF indices

447   In this section, we presented detailed visual comparison results for all the seven PMF indices under

448 three different environmental conditions. High values of the PMFI$_{first}$, PMFI$_{second}$, PMLI$_{swir}$, mPMCI,

449 MBPMFI, and BPMFI correspond to PMF objects, while a high value of the PMLI is related to Non-PMF

450 objects. For the convenience of visual comparisons between the PMLI and the other six indices, the color

451 bar of PMLI was reversed. Consequently, in all seven index images, the red color is associated with PMF,

452 and the blue color is related to Non-PMF.

4.1.1 Visual comparison in Region I

454   In Region I, the MBPMFI and BPMFI indices outperformed the other five indices in highlighting PMF

455 and suppressing background noise (Fig. 8 (g) and (h)). The mPMCI performed the poorest, barely

456 recognizing PMF (Fig. 8 (f)). PMLI and PMLI$_{SWIR}$ showed similar performance, both misclassifying

457   vegetation as PMF. Region I is located in the Hetao Irrigation District of Inner Mongolia, where croplands

458   are extensively irrigated through the integral irrigation systems. The shortwave-infrared spectrum is highly

459   absorbed by water. Although PMF had a higher reflectance value in the red spectrum than vegetation, the

460   wet soil caused by irrigation can lead to lower reflectance values in shortwave-infrared spectrum for

461   vegetation than for PMF. In this context, both PMF and vegetation might exhibit a low reflectance value in

462   PMLI (Eq. (6)), leading to misclassification between them (Zhang et al., 2022g). While $PMLI_{SWIR}$ (Eq. (9))

463   was primarily designed to separate PMF from bare land, it failed to suppress vegetation, which also had a

464   high reflectance value in the near-infrared spectrum and low reflectance value in the shortwave-infrared

465   spectrum similar to PMF (Fig. 8 (e)). $PMFI_{first}$ and $PMFI_{second}$ could highlight PMF to a certain extent, but

466   wrongly highlighted some background objects, such as roads and bare lands (Fig. 8 (c) and (d)). Overall,

467   MBPMFI and BPMFI showed comparable performance in highlighting PMF signals, with BPMFI having

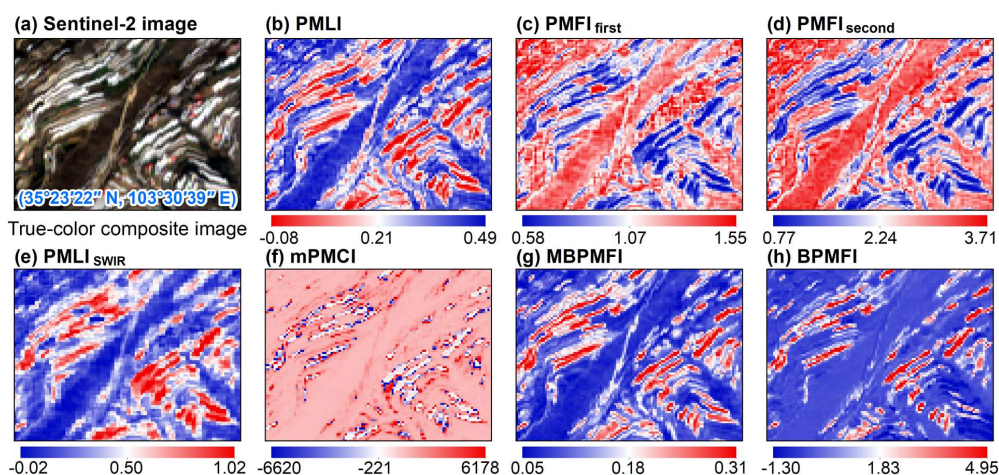468   an advantage in suppressing background noise, especially roads.

469
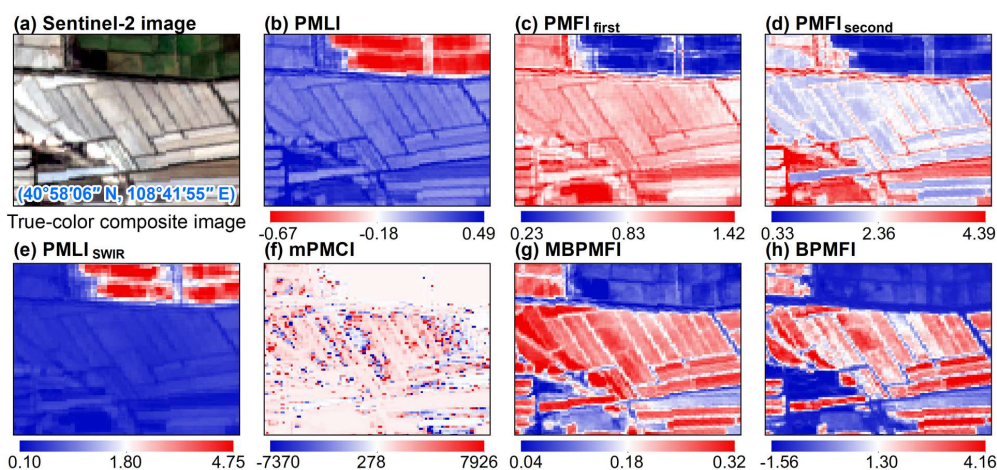
Figure 8.   Visual evaluation results based on the plastic-mulched farmland indices of PMLI (b), $PMFI_{first}$ (c), $PMFI_{second}$
(d), $PMLI_{SWIR}$ (e), mPMCI (f), MBPMFI (g), and BPMFI (h) in a representative area of Bayan Nur City, Inner Mongolia
Province (a). The red color is related to PMF, and the blue color is associated with backgrounds under all of the seven
indices.

4.1.2 Visual comparison in Region II

475   Unlike Region I, Region II is dominated by bare land and PMF, with PMF distributed sparsely in long

476   strips. MBPMFI and BPMFI continued to demonstrate the best performance in highlighting PMF and

477   suppressing background noise (Fig. 9 (g) and (h)). Since PMLI and $PMLI_{SWIR}$ were primarily proposed to

478   differentiate PMF from bare land (Lu et al., 2014; Hao et al., 2019), they could roughly identify PMF but

479   failed to suppress some backgrounds, such as roads and buildings (Fig. 9 (b) and (e)). In contrast to Region

480   I (Fig. 8), the reflectance values of PMF in $PMFI_{first}$ and $PMFI_{second}$ were both lower than those of Non-

481   PMF, indicating that Non-PMF was highlighted, while PMF was suppressed (Fig. 9 (c) and (d)). This was

482   because, compared with bare land, PMF had higher reflectance values in both the blue and near infrared

483   spectra (Xiong et al., 2019; Hasituya et al., 2016; Hao et al., 2019), but no obvious difference was observed

484   in the shortwave-infrared spectrum (Hasituya et al., 2016). Consequently, PMF might have lower values in

485     $PMFI_{first}$ and $PMFI_{second}$ than bare land. The mPMCI continued to exhibit the poorest performance among

486   the seven indices (Fig. 9 (f)). Compared with MBPMFI, BPMFI was more effective in suppressing Non-

487   PMF land covers, such as bare land and buildings (Fig. 9 (g) and (h)). In general, BPMFI still performed

488   the best in Region II.

Figure 9. Visual evaluation results based on the plastic-mulched farmland indices of PMLI (b), $PMFI_{first}$ (c), $PMFI_{second}$ (d), $PMLI_{SWIR}$ (e), mPMCI (f), MBPMFI (g), and BPMFI (h) in a representative area of Linxia City, Gansu Province (a). The red color is related to PMF, and the blue color is associated with backgrounds under all of the seven indices.

493   **4.1.3 Visual comparison in Region III**

494   Differing from Region I and Region II, Region III featured a more complex background environment,

495   including PMF, vegetation, bare land, buildings, and plastic greenhouses. Among the seven indices, BPMFI

496   demonstrated the best performance in identifying PMF and suppressing background noise (Fig. 10 (h)).

497   While PMLI, $PMFI_{first}$, and MBPMFI were also able to highlight PMF, they failed to effectively suppress

498   certain background elements, particularly buildings and plastic greenhouses (Fig. 10 (b), (c), and (g)).

499     $PMFI_{second}$ and $PMLI_{SWIR}$ seemed to wrongly highlight backgrounds while suppressing PMF (Fig. 10 (d)

500   and (e)). The mPMCI continued to perform the worst in recognizing PMF (Fig. 10 (f)). Overall, BPMFI

501   effectively separated PMF from background elements, whereas PMF detected by other indices was easily

502   confused with the background.

503   The evaluation results indicated that BPMFI had the highest robustness in identifying PMF under

504   various environmental conditions. It could more effectively highlight PMF and suppress Non-PMF than the

505   other six indices. The performance of MBPMFI ranked only next to BPMFI. Although MBPMFI was useful

506   for identifying PMF in Region I and Region II, it failed to suppress the complex backgrounds in Region III.

507   The other five indices were only effective in identifying PMF in specific regions, lacking the capability to

508   consistently recognize PMF under complicated background conditions.
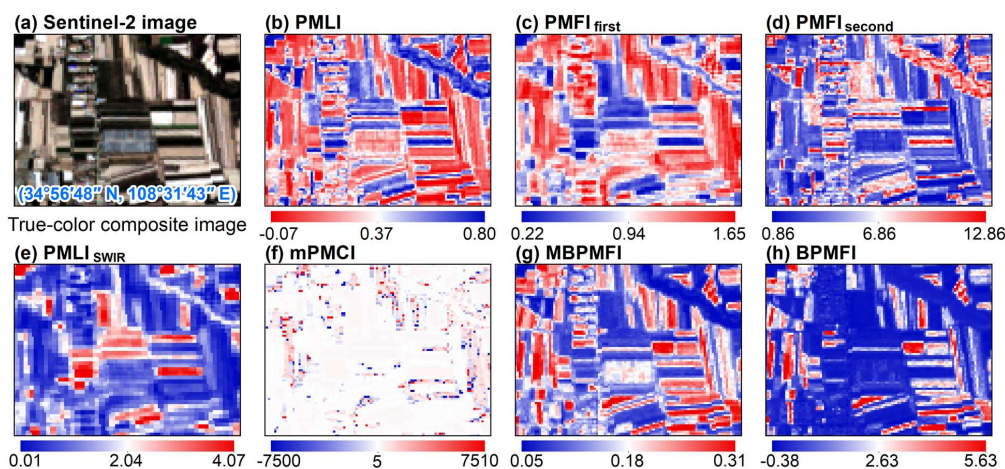
509
510   **Figure 10.**   Visual evaluation results based on the plastic-mulched farmland indices of PMLI (b), PMFI$_{first}$ (c), PMFI$_{second}$
511   (d), PMLI$_{SWIR}$ (e), mPMCI (f), MBPMFI (g), and BPMFI (h) in a representative area of Xianyang City, Shaanxi Province
512   (a). The red color is related to PMF, and the blue color is associated with backgrounds under all of the seven indices.

513   **4.2 Classifier performance for the transferability scenarios**

514   All locally adaptive classifiers in the reference scenario (Scenario–Ref) showed satisfactory accuracy

515   in PMF mapping (Fig. 11 (a)). In this scenario, the F1 values of PMF ranged from 0.64 to 0.94, with an

516   average of 0.85. For all cities, the F1 values were close to or above 0.80, except in the NID (0.75), Baotou

517   (0.75), Hohhot (0.64), and Ordos (0.73). The high F1 values indicated that the locally adaptive classifiers

518   trained in this study can meet the practical demands for actual PMF mapping.

519   The F1 values from each transferability scenario (Scenario–T, Scenario–ST) were compared with

520   those from the reference scenario (Scenario-Ref) in each city, and the percentage change in the F1 values

521   (F1$_{change}$) was also computed (Fig. 11 (b) and (c)). Generally, the comparison results showed that for all

522   cities, the F1 values decreased from the Scenario–Ref to Scenario–ST in an orderly manner (Scenario–ST >

523   Scenario–T > Scenario–Ref). In Scenario–T (Fig. 11 (b)), the average F1$_{change}$ was -2.92% for 2019 and -

524   6.07% for 2021. Except in Qinghai, Datong, and Yangquan, where the F1$_{change}$ values were below -20% in

525   2021, the F1$_{change}$ values for all other cities were above -20%. In Scenario–ST (Fig. 11 (c)), the average

526   F1$_{change}$ was -13.86% for 2019 and -21.94% for 2021, which was absolutely 10.94% and 15.87% lower than

527   in Scenario–T for 2019 and 2021, respectively. Furthermore, one-third of the cities in the Loess Plateau

528   showed a percentage decline in the F1 values over -20% in Scenario–ST. The greater decrease in F1 values

529   in Scenario–ST compared to Scenario–T indicated that Scenario–ST was hardly suitable for the mapping

530   of PMF distributions across different years.

531
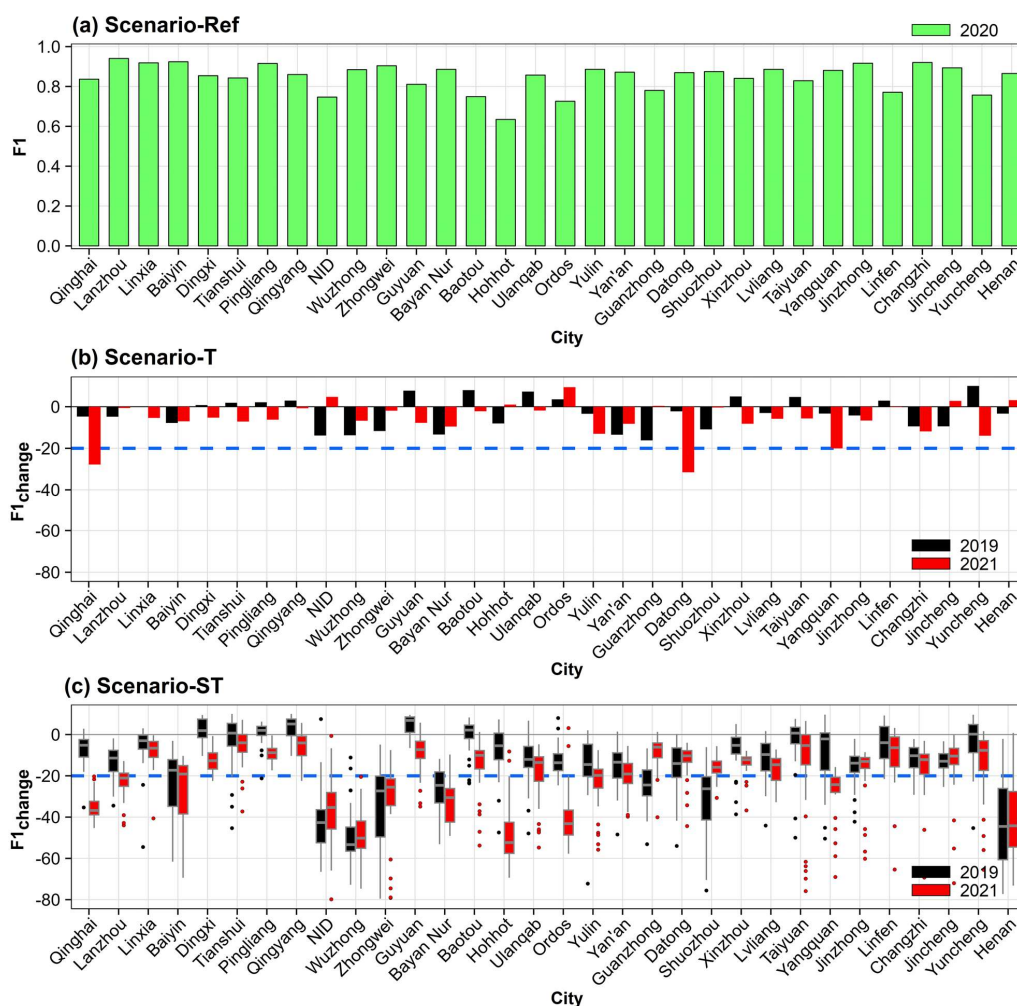
Figure 11.   Transferability evaluation of the pre-trained classifiers for plastic-mulched farmland (PMF) mapping. (a) F1

values of PMF mapping based on locally adaptive classifiers trained with data in 2020 in each city of the Loess Plateau

(Scenario–Ref). (b) Percentage change of F1 values (F1$_{change}$) for temporal transferability scenario (Scenario–T). (c)

F1$_{change}$ for spatial–temporal transferability scenario (Scenario–ST).

4.3 Accuracy assessment for resultant maps

537   Given the strong performance of the temporal classifier transfer (Scenario–T) in multi-year PMF

538   mapping, classifiers trained on automatically generated samples and optimal features in 2020 were

539   exploited to mapping PMF distributions (PMF-LP) for 2019–2021. The accuracy assessment for the three

540   years was implemented based on the validation samples of the entire study area (Table 3). The OA of the

541   resultant maps for all three years varied from 0.82 (2021) to 0.87 (2020). PMF was accurately identified,

542 with F1 values ranging from 0.80 in 2021 to 0.86 in 2020, averaging 0.83 over the three years. For all three-

543 year classification results, PMF exhibited higher PA than UA, indicating that commission errors in PMF

544 recognition were higher than the omission errors. The higher commission errors indicated that some Non-

545 PMF pixels were incorrectly classified as PMF, potentially leading to an overestimation of PMF areas.

546 Detailed pixel-wise accuracy assessments for each city in the Loess Plateau were presented in Table S4~S6.

547

548 **Table 3.**

549 Confusion matrix of the plastic-mulched farmland maps of the Loess Plateau (PMF-LP) for the year 2019–2021. Reference

550 categories are rows while map categories are columns. The numbers in the confusion matrix are the number of ground

551 reference samples. The producer accuracy (PA), user accuracy (UA), F1-score (F1), and overall accuracy (OA) were also

552 displayed in the table. PMF: Plastic-mulched Farmland, Non-PMF: Non-plastic-mulched Farmland.

Year		PMF	Non-PMF	PA	UA	F1	OA
2019	PMF	2685	414	0.87	0.79	0.83	0.84
	Non-PMF	714	3278	0.82	0.89	0.85	
2020	PMF	4678	664	0.88	0.84	0.86	0.87
	Non-PMF	918	5880	0.87	0.90	0.88	
2021	PMF	2468	455	0.84	0.76	0.80	0.82
	Non-PMF	768	3023	0.80	0.87	0.83	

553

554 The estimated areas derived from our maps were compared with the statistical data from yearbooks of

555 12 cities for 2019–2021 (Fig. 12). The PMF areas derived from our maps exhibited high consistency with

556 the statistics, with coefficients of determination (R^2) of 0.92, 0.93, and 0.87 for the year 2019, 2020, and

557 2021, respectively. Notably, the resultant maps for 2021 (Fig. 12 (c)) tended to overestimate PMF areas

558 compared to the statistics, particularly in Qinghai and northern Shanxi, likely due to snow and cloud

559 residuals being misclassified as PMF (discussed in Section 5.3). The strong consistency between the

560 estimated areas and the statistical data underscored the reliability of the maps produced in this study.
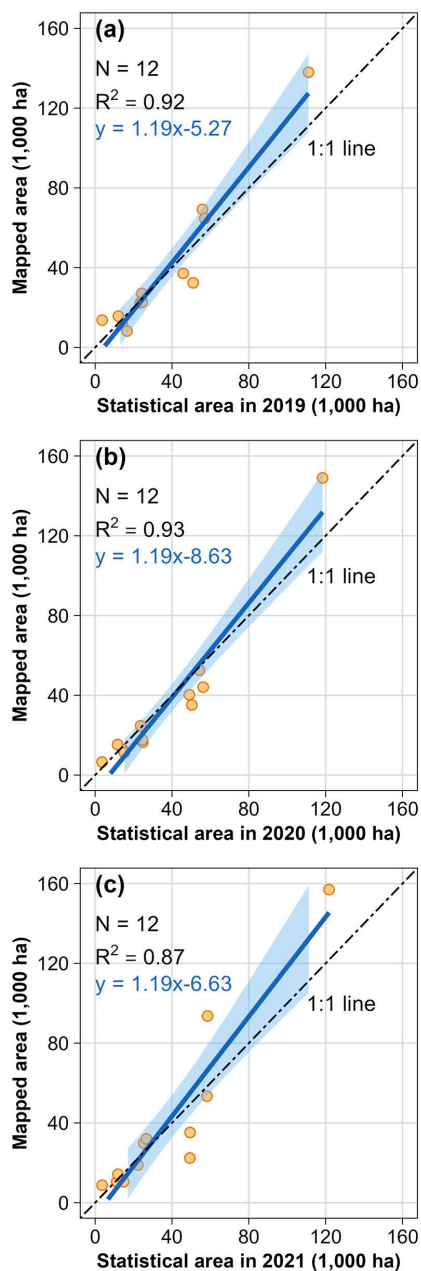
Figure 12. Comparison of the mapped PMF (Plastic-mulched Farmland) areas with the statistics for 12 cities with PMF area statistics for the year 2019 (a), 2020 (b), and 2021 (c).
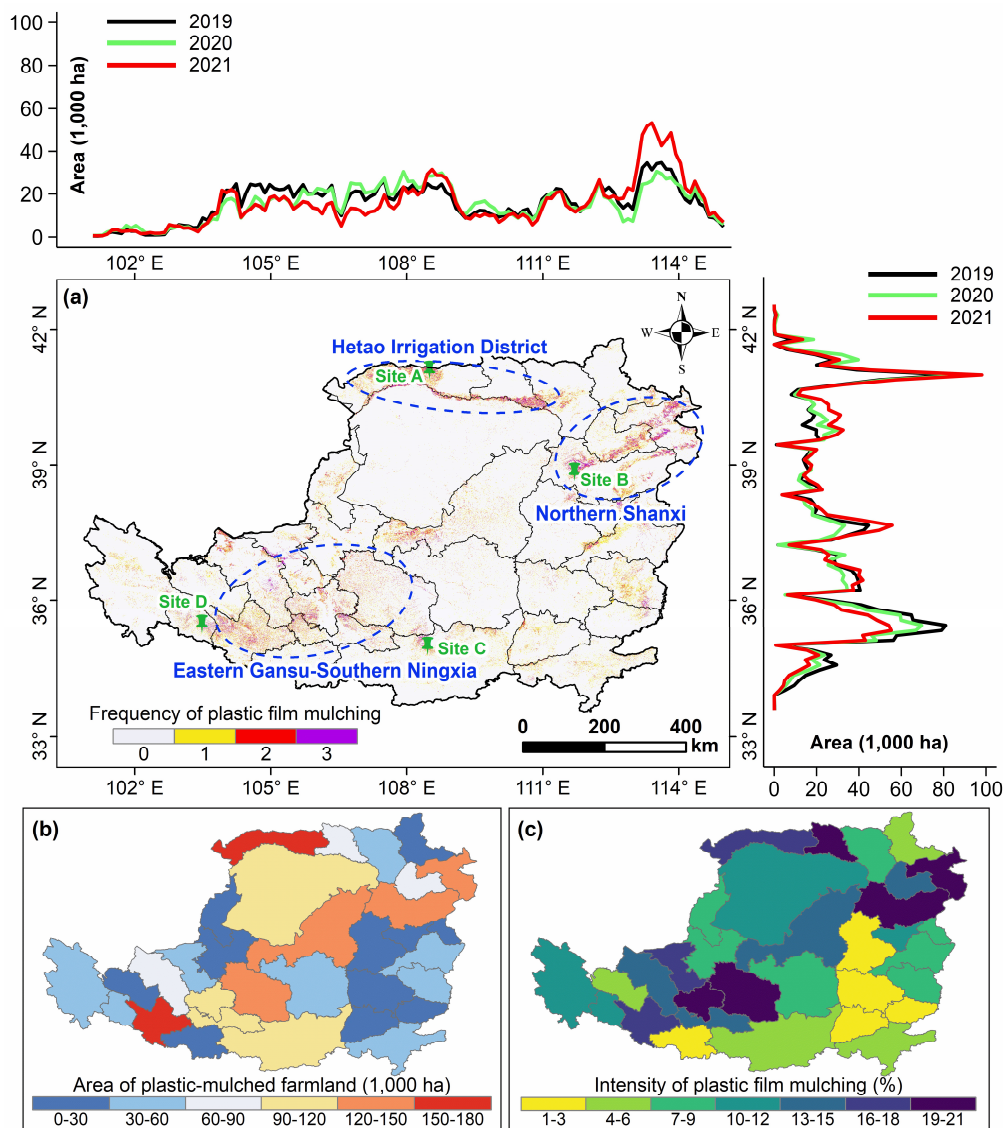
4.4 Spatial distributions of PMF

The final PMF mapping results were shown in Fig. 13. To quantify the intensity of plastic film usage across different cities in the Loess Plateau, we calculated the ratio of plastic-mulched area (derived from

567   the resultant maps) to the total cultivated land area (derived from cropland layers in Section 2.2.2) for each

568   city (Fig. 13 (c)). PMF was widely distributed across the Loess Plateau, exhibiting a pattern of extensive

569   dispersion and localized clustering (Fig. 13 (a)). The Hetao Irrigation District, including the Bayan Nur and

570   Baotou cities in Inner Mongolia Province, exhibited the highest intensity of plastic film usage at 18%,

571   followed by Northern Shanxi (including Datong, Shuozhou, and Xinzhou) at 17%, and the Eastern Gansu-

572   Southern Ningxia region (including Dingxi, Baiyin, Pingliang, Qingyang, Zhongwei, and Guyuan) at 16%

573   (Fig. 13 (c)). In these arid and cold regions, plastic films have been extensively used for decades to ensure

574   crop yields by regulating temperature and conserving moisture (Wang et al., 2022a; Yan et al., 2014; Zhao

575   et al., 2023). The total PMF areas for each 0.10° longitude and latitude bin were also presented on the top

576   and right sides of the 2020 resultant map (Fig. 13 (a)). Plastic film was extensively used in latitude ranges

577   of 35°–37° N and 40°–41° N, and in the longitude ranges of 106°–109° E and 112°–114° E. However,

578   plastic film usage in the latitude range of 38°–40° N and longitude range of 109°–111° E was comparatively

579   lower than other regions. This disparity could be attributed to the prevalent local land cover types in Ordos

580   of Inner Mongolia Province, where grassland and bare land account for about 90% of the total area (Zhang

581   et al., 2021c; Yang and Huang, 2021).

582   To further validate the PMF mapping results, a more detailed visual evaluation was conducted by

583   selecting representative areas in different years (Fig. 14). Obviously, PMF was effectively distinguished

584   from other land cover types, regardless of various cropland sizes and shapes. In site A, Bayan Nur, Inner

585   Mongolia Province, PMF was densely distributed in regular rectangles (Fig. 14 (a)). There were clear

586   separations between PMF and roads in the mapping results. When the classifiers trained in 2020 were

587   applied to 2019 and 2021, some PMF pixels in site A were not identified in 2019 (Fig. 14 (b)), while in

588   2021, there were instances of erroneously classifying Non-PMF pixels as PMF (Fig. 14 (f)). Site B in

589   Xinzhou of Shanxi Province, had large fields with irregular shapes compared to site A (Fig. 14 (g))

590   compared with site A. The PMF mapping results from 2019 to 2021 at this site showed strong spatial

591   agreement with the Sentinel-2 true-color composite images (Fig. 14 (h), (j), and (l)). In site C, Xianyang,

592   Shaanxi Province, PMF was scattered among winter crops (Fig. 14 (m)). The mapping results showed good

593   separability between winter crops and PMF across different years (Fig. 14 (n), (p), and (r)). For site D in

594   Linxia of Gansu Province, the cultivated farmland was primarily characterized by terraced fields, presenting

595   elongated and irregular shapes (Fig. 14 (s)). These terraced fields were interspersed with vegetations,

596   buildings, and bare lands. The mapping results were also satisfactory in this site (Fig. 14 (t), (v), and (x)).

Figure 13. Spatial patterns of plastic-mulched farmland (PMF) in the Loess Plateau from 2019 to 2021. (a) Frequency of plastic film mulching. The blue dashed ellipses represent the regions with dense distributions of PMF. Site A, B, C, and D are the zoom-in view cases in Fig. 14. (b) Area of PMF in each city in 2020. (c) Intensity of plastic film mulching in 2020 across various cities. Intensity of plastic film mulching is defined as the ratio of PMF area to total cultivated area.
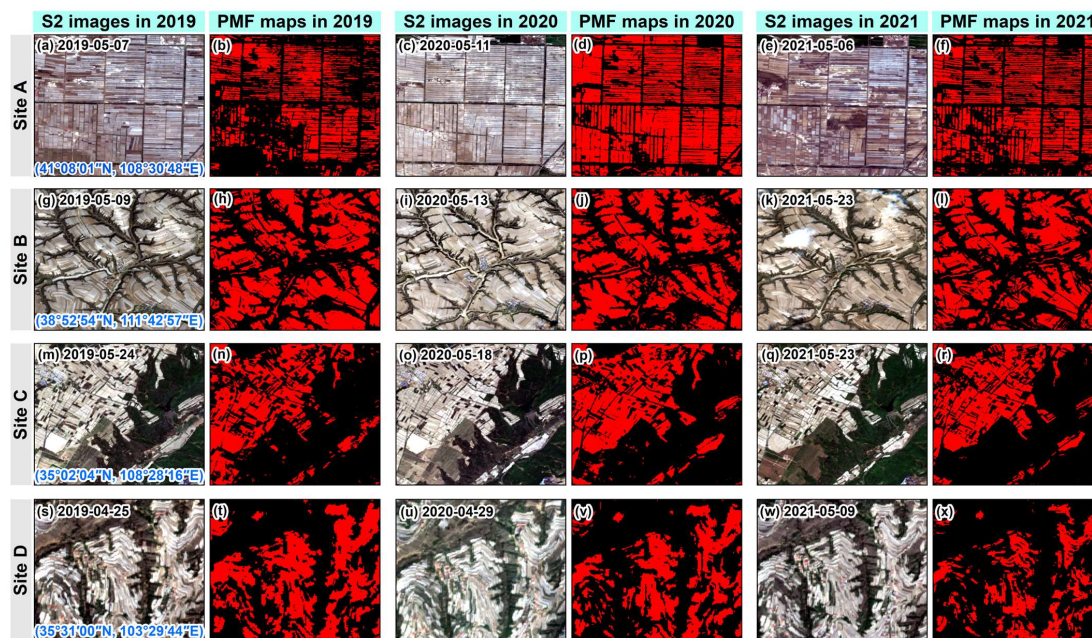
Figure 14. Spatial details of the plastic-mulched farmland (PMF) map subsets from different regions in the years of 2019, 2020, and 2021. Site A, B, C, and D correspond to the four typical regions marked in Fig 13. The 1st, 3rd, and 5th columns are the Sentinel-2 (S2) images with a true-color composite of red, green, blue bands in the years of 2019, 2020, and 2021, respectively. The 2nd, 4th, and 6th columns are the PMF maps established in this study.

5   Discussion

5.1 Feasibility of MBPMFI and BPMFI for automatic training sample generation

Image sources, algorithms, and training samples are three crucial factors influencing any land cover classification task (Huang et al., 2020; Wen et al., 2022; Zhang et al., 2021b). The advancement of remote sensing technology has provided access to massive open datasets and powerful cloud-based computing platforms (Song et al., 2017; Yang et al., 2019; Tamiminia et al., 2020). However, large-scale and multi-year land cover classification is still constrained by the lack of training samples (Huang et al., 2020; Wen et al., 2022). This issue is particularly pronounced for land cover types like PMF, which have received less attention in the past, making training sample collection more challenging. To address this gap, we developed two novel indices, MBPMFI and BPMFI, to automatically generate training samples. Compared with traditional field surveys and visual interpretation, the proposed indices offer a more convenient and labor-saving alternative for obtaining training samples. The prior information, such as mulching and flourishing dates, is not strictly time-specific and can be easily obtained from local management experiences and relevant studies. Furthermore, because the two indices rely solely on the blue band, their calculation is simple and fast.

622 Additionally, the visual comparison results under various environmental conditions in this study
623 demonstrated the superior robustness of MBPMFI and BPMFI over the other existing indices in
624 highlighting PMF signals and suppressing background noises. Previous studies have shown that PMF can
625 be effectively distinguished from other land cover types across the visible to shortwave-infrared spectrum
626 during the mulching stage (Lu et al., 2014; Hasituya et al., 2016; Hao et al., 2019). However, PMF indices
627 based solely on optical images from the mulching stage often struggle to differentiate PMF from bare land
628 and impervious surfaces (Lu et al., 2014; Hao et al., 2019) (Fig. 6 (e)~(h)), which limits their applicability
629 in complex environments. In this study, we considered PMF characteristics across the pre-mulching,
630 mulching, and flourishing stages to develop two novel PMF indices. Both indices exhibited greater
631 robustness than the existing ones in distinguishing PMF from various complex backgrounds. Of the two
632 indices, BPMFI was more effective in highlighting PMF signals and suppressing background noise, making
633 it particularly promising for rapid and precise PMF recognition in areas with seamless satellite imagery.
634 However, because the calculation of BPMFI requires images from three different periods, which might be
635 unavailable in cloudy regions, MBPMFI is more practical for PMF recognition when only mulching-stage
636 images are available. To further improve the quality of training samples in this study, we collected samples
637 classified as PMF by both indices, and then conducted strict spatial filtering. The high PMF mapping
638 accuracy (F1 = 0.86) and the strong correlation (R^2 = 0.93) between estimated and statistical PMF areas in
639 2020 confirm the quality of these training samples.

640 **5.2 Threshold stability of the MBPMFI and BPMFI**

641 Threshold used for index-based classification is typically determined using statistical data (Zhang et
642 al., 2022e; Zhang et al., 2022b), ground truth data (Zhang et al., 2022g; Zhou et al., 2024), or automatic
643 threshold determination methods (Yang et al., 2023). In this study, we employed ground truth samples from
644 rectangular regions (Fig. 1 (a)) to determine the threshold for each province of the Loess Plateau, because
645 statistical data were not available in most cities and automatic methods could require significant
646 computational resources at large scales. To evaluate the stability of MBPMF and BPMFI thresholds, we
647 tested the mapping accuracy in the rectangular regions based on thresholds -50%–50% off the best threshold
648 (Fig. 15). Compared with MBPMFI, BPMFI can achieve more stable performance even with a threshold
649 largely off from the best threshold. The F1 values ranged from 0 to 0.98 for MBPMFI and from 0.80 to
650 0.97 for BPMFI with the thresholds ±50% off from the best threshold across all regions. The stable F1
651 values of BPMFI indicated that it is not sensitive to threshold variations, which makes it well-suited for
652 large-scale PMF mapping.
653 According to the results of our study, the best BPMFI threshold was 0.40 for Qinghai, Shaanxi, and

654   Shanxi, and 0.80–1.10 for Gansu, Ningxia, and Inner Mongolia. The relatively large difference in the best

655   thresholds may be attributed to variations in plastic materials (Xiong et al., 2019; Zhang et al., 2022g) and

656   crop species grown in the fields. The former affects the peak reflectance of PMF during the mulching stage,

657   and the latter influences the absorption of the visible spectrum during the flourishing stage. The more

658   detailed relationship between these factors and the spectral signatures of PMF deserves to be explored in

659   the future. Additionally, based on the threshold stability assessment in Fig. 15, we recommend using a

660   BPMFI threshold of 0.40–0.60 (i.e., approximately 50%–150% of the optimal threshold) and an MBPMFI

661   threshold of 0.14–0.15 (i.e., approximately 90%–110% of the optimal threshold) for PMF recognition

662   across the entire Loess Plateau. But for high-precision PMF mapping, it is suggested to segment the whole

663   area into sub-regions and determine the optimal thresholds separately for each region.
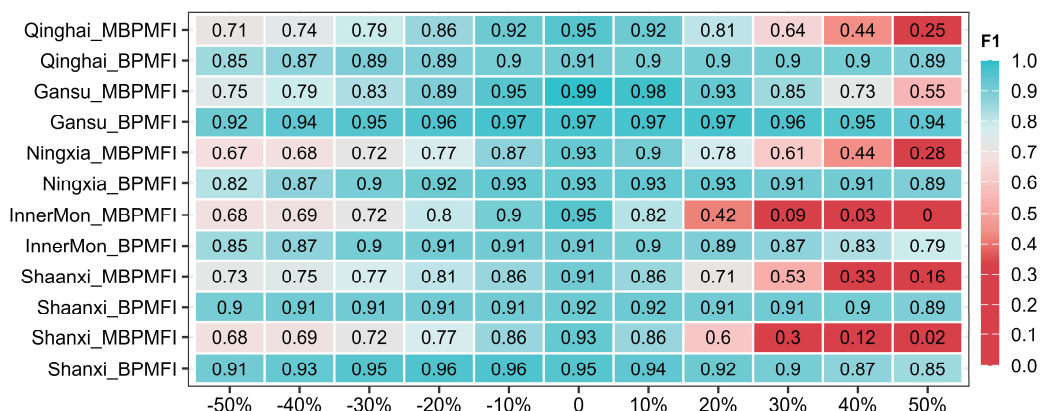
664

665   **Figure 15.** Plastic-mulched farmland (PMF) mapping accuracies (F1-score) based on thresholds -50%–50% off the best

666   threshold in the two novel PMF indices of MBPMFI and BPMFI. "±n%" indicates threshold = best threshold ±n% × best

667   threshold.

5.3 Feasibility and error of classifier transfer for PMF mapping

669   Classifiers, pre-trained in specific areas/years with sufficient samples, have great potential for rapid

670   land cover and crop type mapping in new areas/years where training data are lacking (Ma et al., 2024).

671   Previous studies on classifier transfer primarily focused on crop type mapping (Wang et al., 2019; Hao et

672   al., 2020; Yang et al., 2023). In contrast, ground reference samples for PMF are more limited, and the

673   feasibility of employing classifier transfer for PMF mapping has not been thoroughly explored.

674   Understanding the extent of performance loss in classifier transfer is crucial for large-scale and multi-year

675   PMF mapping. Therefore, this study quantitatively evaluated the performance loess when the trained

676   classifier is directly applied in two transferability scenarios (Scenario–T, Scenario–ST) for PMF mapping.

677   The findings demonstrated decreased performance in both transferability scenarios compared to the no-

678   transfer case (Scenario–Ref). The temporal classifier transfer (Scenario–T) was more suitable for retracing

679   historical PMF distributions than spatial–temporal classifier transfer (Scenario–ST), with percentage

680   changes in F1 being less than 7.0% on average compared to the no-transfer case. Several potential factors

681   that may cause performance reduction in Scenario–T and Scenario–ST (Fig. 11) could be categorized into

682   three main groups: (1) missing clear Sentinel-2 data during the mulching stage; (2) snow and cloud residual

683   contaminations during the pre-mulching stage; and (3) variations in mulching dates across different regions

684   and years.

685   First, high-quality Sentinel-2 data during the mulching stage is crucial for enlarging the inter-class

686   variations between PMF and Non-PMF as illustrated in Section 3.1.2. Particularly, the local peak values in

687   the blue band of time-series Sentinel-2 (i.e., Blue_peak) is the most important feature for PMF mapping

688   (Fig. 7). Missing data during the mulching stage could result in the disappearance or distortion of the local

689   peak values, causing classifiers trained on regions/years with high-quality data to fail in mapping PMF in

690   regions/years with missing data. For example, during the mulching stage, more than half of the pixels in

691   Qingyang had more than four clear-sky observations (Fig. 16 (a)), while nearly 75% of the pixels in Henan

692   had fewer than three clear-sky observations (Fig. 16 (b)). Consequently, the local peaks of the harmonic

693   regression curves in Henan (Fig. 16 (e)) were lower than those in Qingyang (Fig. 16 (d)) during 2019–2021,

694   which led to low accuracy when using classifiers trained with Qingyang data from 2020 to recognize PMF

695   in Henan for 2019 (F1 = 0.64) and 2021 (F1 = 0.49). Although the Sentinel-2 satellite provides data with a

696   5-day revisit cycle and cloud contamination in northern China is less severe than in southern China, the

697   observable duration of plastic film is short and influenced by crop canopy, which leads to the unavailability

698   of images containing plastic film signals. Multi-sensor satellite data could be employed to increase the

699   density of observations to account for this limitation.

700   Next, clouds and snow, which exhibit similar bright characteristics in all visible bands as PMF, are

701   difficult to be thoroughly masked out using only the quality assessment (QA) bands of Sentinel-2 (You and

702   Dong, 2020). For example, although the percentage of clear-sky observations in Qinghai was the same as

703   in Qingyang (Fig. 16 (a) and (c)), snow and cloud residuals distorted the harmonic regression curves in

704   Qinghai in 2021 (Fig. 16 (f) and (g)), leading to the performance loss when using classifiers trained with

705   Qinghai (or other city) data from 2020 to recognize PMF in the same region for 2021 (Fig. 11 (b) and (c)).

706   To mitigate the negative effects of clouds and snow on classifier transfer for PMF mapping, more effective

707   cloud detection algorithms should be implemented. Inspired by You and Dong (2020), two spectral indices

708   (Normalized Difference Moisture Index (NDMI) and Normalized Difference Snow Index (NDSI)) could

709   be used to mask out clouds to improve the performance of classifier transfer in the future.

710   Finally, variations in sowing dates of plastic-mulched crops among different regions could lead to

711   changes in mulching dates, which in turn affect the occurrence dates of local peaks and the shape of

712   harmonic regression curves. In this study, in the Ningxia Irrigation District (NID, Fig. S1) and Wuzhong of

713   Ningxia Province, mulching dates were earlier than in other cities (Fig. S11) due to the widespread

714   cultivation of watermelon, which is mainly sown in March. Consequently, the performance exhibited a

715   significant decrease (median $F1_{change} \approx$ -50%) when using classifiers trained with data from other city in

716   2020 to recognized PMF in the two cities (Scenario–ST) for 2019 and 2021.

717   Apart from the main factors mentioned above, climate variables (e.g., rainfall, temperature), farming

718   practices (e.g., sowing and harvesting practices), technological evolution, and policy implementation could

719   also impact the mulching practices, which may adversely affect the performance of classifier transfer. The

720   links between classifier transferability and these factors require further exploration. Additionally, multi-

721   year/multi-region data have been employed to enhance classifier transferability for crop type mapping

722   (Wijesingha et al., 2024; Orynbaikyzy et al., 2022; Luo et al., 2022). Considering the increasing focus on

723   PMF mapping (Veettil et al., 2023), there will likely be more training data from different years and regions

724   available to develop more generalized classifiers for PMF mapping in the future.

725
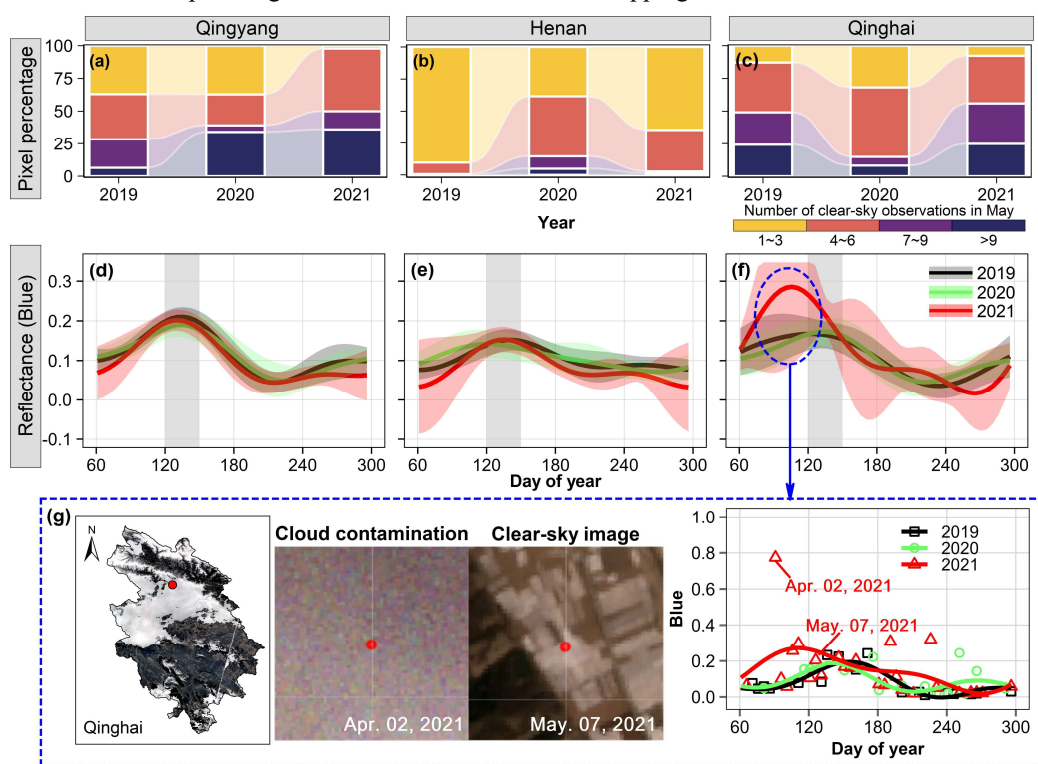
Figure 16.   Explanations for the failures of Plastic-mulched farmland (PMF) mapping caused by data missing and cloud contamination. (a)~(c) Percentage of clear-sky observations at each cropland pixel during the mulching stage in Qingyang, Henan, and Qinghai. (d)~(f) Harmonic regression curves of PMF in Qingyang, Henan, and Qinghai for the year 2019, 2020 and 2021. The gray buffer represents mulching period. The black, green, and red buffers indicate one standard deviation. (g) A representative example in Qinghai for depicting the adverse effects of snow and clouds on PMF mapping.

731

5.4 Advantages and uncertainties of the new framework

In this study, we proposed a new framework that combines index-based methods with supervised classifier transfer for large-scale PMF mapping. This framework offers two main advantages. First, we introduced two novel and robust PMF indices (MBPMFI and BPMFI) for generating training samples, significantly enhancing the efficiency of sample collection compared to field surveys and visual interpretation. Second, temporally transfer pre-trained classifiers to mapping multi-year PMF distributions further facilitates the long-term PMF monitoring without training domain- and year-specific classifiers. The automatic generation of training samples and classifier transfer make this framework highly promising for rapidly mapping large-scale and multi-year PMF distributions in practice. The satisfactory mapping accuracy of PMF (F1 > 0.80) in the Loess Plateau during 2019–2021 further demonstrated the reliability of this framework. Additionally, since the reflectance bands used for training sample generation and feature extraction are similar to those of Landsat satellites, this framework is also believed to be applicable for PMF mapping with Landsat data.

Although the new framework successfully identified PMF across different regions and years in the Loess Plateau of China, there still exists some room for improvement. First, two different cropland layers from 2020 were integrated to exclude the non-cropland pixels for 2019–2021 before PMF recognition. However, errors in these products may affect PMF mapping results. For instance, unrecognized cropland pixels in the products could lead to the loss of potential PMF pixels, thereby increasing the omission errors in the PMF mapping results. One possible solution is to integrate more state-of-the-art land cover products (Tu et al., 2024; Zhang et al., 2024) to enhance the reliability of the cropland mask.

Next, although Sentinel-2 has a 5-day revisit cycle, clear-sky observations are still often limited in some regions, especially in southern China, due to inevitable cloud contaminations. The large-scale loss of images during the mulching stage could constrain the application of the proposed framework. To address this issue, more optical satellite imagery, such as Landsat-4/5/7/8/9, could be integrated to provide denser time-series observations in the future. Furthermore, this study did not include radar data which is impervious to atmospheric interference in PMF mapping. Incorporating radar data for PMF mapping will be the next step of our research.

Third, this study focused on evaluating temporal and spatial-temporal transferability of the RF classifier for PMF mapping. Due to the limitations of GEE platform, deep learning algorithms such as Deep Neural Network (DNN) and Convolution Neural Network (CNN), which exhibit better performance than the traditional supervised classifiers (Zhong et al., 2019; Wang et al., 2021), were not explored in this study. However, employing deep learning algorithms for PMF mapping presents challenges related to

764 computational costs and the need for more training data (Xu et al., 2021; Zhang et al., 2020a; Wijesingha

765 et al., 2024).

766 **6 Data availability**

767 The PMF-LP product generated in this paper is openly available at

768 https://doi.org/10.5281/zenodo.13369426 (Zhao et al., 2024). The dataset includes a set of GeoTIFF images

769 in the EPSG:4326 spatial reference system. The value 0 and 1 represent PMF and Non-PMF, respectively.

770 We encourage users to independently verify the PMF maps.

771 **7 Conclusions**

772 Plastic film mulching technology can effectively enhance crop yield, but also poses significant

773 environmental issues, such as "white pollution" and soil microplastic contamination. Unfortunately, there

774 is no method currently available for the rapid and automated mapping of plastic-mulched farmland (PMF)

775 across large areas and multiple years. In this study, to address the challenge of lacking ground reference

776 samples to train supervised classifiers, we developed an automatic training sample generation method based

777 on two newly proposed PMF indices: MBPMFI and BPMFI. To rapidly retrace historical PMF distributions,

778 we thoroughly explored the spatial–temporal transferability of pre-trained classifiers and the factors

779 influencing their transferability. Finally, PMF distribution maps for the Loess Plateau of China were

780 produced by integrating the automatic training sample generation method with the classifier transfer

781 approach.

782 The results of this study indicated that the novel PMF indices, MBPMFI and BPMFI, outperformed

783 the existing PMF indices in PMF recognition. The novel indices could not only highlight PMF information

784 but also suppress complex background signals under various environmental conditions. Temporal classifier

785 transfer (Scenario–T) showed great potential for rapid mapping of multi-year PMF distributions in regions

786 and years lacking ground reference samples, with an average performance loss less than 7.0% compared to

787 the locally adaptive classifiers. Based on the index-based training samples generation method and classifier

788 transfer, PMF distributions were generated across the Loess Plateau (PMF-LP) and achieved satisfactory

789 accuracy, with F1 values of 0.83, 0.86, and 0.80 for 2019, 2020, and 2021, respectively. The estimated PMF

790 areas also agreed well with the municipal-level agricultural census data ($R^2 \geq 0.87$). In summary, the newly

791 proposed PMF mapping framework has great potential to rapidly mapping PMF distributions across large

792 areas and multiple years. Future work will apply this framework to monitor the spatiotemporal dynamics

793 of PMF distributions in China.

794

Supplement.

The supplement related to this article is available online at: https://doi.org/

Author contributions.

CZ and JH conceptualized the study. CZ designed and carried out the experiment. CZ wrote the original manuscript. YL, XC, and LW collected dataset and implemented formal analysis. ZW, HF, and QY provided direction and comments. JH was responsible for funding acquisition. All authors discussed the results and revised the manuscript.

Competing interests.

The contact author has declared that none of the authors has any competing interests.

Disclaimer.

Publisher's note: Copernicus Publications remains neutral with regard to jurisdictional claims in published maps and institutional affiliations.

Acknowledgements.

The author gratefully acknowledgements all data providers whose data have been used in this study. Then we thank the support of the Google Earth Engine platform, which provided essential data and computational resources for this study.

Financial support

References

Beck, H. E., McVicar, T. R., Vergopolan, N., Berg, A., Lutsko, N. J., Dufour, A., Zeng, Z., Jiang, X., van Dijk, A. I., and Miralles, D. G.: High-resolution (1 km) Köppen-Geiger maps for 1901–2099 based on constrained CMIP6 projections, Sci. Data, 10, 724, https://doi.org/10.1038/s41597-023-02549-6, 2023.

Belgiu, M. and Drăguţ, L.: Random forest in remote sensing: A review of applications and future directions, ISPRS J. Photogramm. Remote Sens., 114, 24-31, https://doi.org/10.1016/j.isprsjprs.2016.01.011, 2016.

Breiman, L.: Random forests, Mach. Learn., 45, 5-32, 2001.

Chaves, M. E. D., Picoli, M. C. A., and Sanches, I. D.: Recent applications of Landsat 8/OLI and Sentinel-2/MSI for land use and land cover mapping: A systematic review, Remote Sens., 12, 3062, https://doi.org/10.3390/rs12183062, 2020.

Cheng, L., Fu, C., Xi, H., Chang, L., Li, S., and Qin, S.: Spatiotemporal variations of plastic-mulched cropland in Hexi Corridor using multi-source remote sensing data (in Chinese), Transactions of the Chinese Society of Agricultural Engineering,

827   39, 124-131, https://doi.org/10.11975/j.issn.1002-6819.202303209, 2023.

828   Defourny, P., Bontemps, S., Bellemans, N., Cara, C., Dedieu, G., Guzzonato, E., Hagolle, O., Inglada, J., Nicola, L., Rabaute, T.,
829   Savinaud, M., Udroiu, C., Valero, S., Bégué, A., Dejoux, J.-F., Harti, A. E., Ezzahar, J., Kussul, N., Labbassi, K.,
830   Lebourgeois, V., Miao, Z., Newby, T., Nyamugama, A., Salh, N., Shelestov, A., Simonneaux, V., Traore, P. S., Traore,
831   S. S., and Koetz, B.: Near real-time agriculture monitoring at national scale at parcel resolution: Performance assessment
832   of the Sen2-Agri automated system in various cropping systems around the world, Remote Sens. Environ., 221, 551-
833   568, https://doi.org/10.1016/j.rse.2018.11.007, 2019.

834   Deng, C. and Wu, C.: BCI: A biophysical composition index for remote sensing of urban environments, Remote Sens. Environ.,
835   127, 247-259, https://doi.org/10.1016/j.rse.2012.09.009, 2012.

836   Drusch, M., Del Bello, U., Carlier, S., Colin, O., Fernandez, V., Gascon, F., Hoersch, B., Isola, C., Laberinti, P., and Martimort,
837   P.: Sentinel-2: ESA's optical high-resolution mission for GMES operational services, Remote Sens. Environ., 120, 25-
838   36, https://doi.org/10.1016/j.rse.2011.11.026, 2012.

839   Farr, T. G., Rosen, P. A., Caro, E., Crippen, R., Duren, R., Hensley, S., Kobrick, M., Paller, M., Rodriguez, E., Roth, L., Seal, D.,
840   Shaffer, S., Shimada, J., Umland, J., Werner, M., Oskin, M., Burbank, D., and Alsdorf, D.: The shuttle radar topography
841   mission, Rev. Geophys., 45, https://doi.org/10.1029/2005RG000183, 2007.

842   Feng, Q., Niu, B., Zhu, D., Yao, X., Liu, Y., Ou, C., Cheng, B., Yang, J., Guo, H., and Liu, J.: A dataset of remote sensing-based
843   classification for agricultural plastic greenhouses in China in 2019 (in Chinese), China Scientific Data, 6,
844   https://doi.org/10.11922/noda.2021.0009.zh, 2021.

845   Fisette, T., Rollin, P., Aly, Z., Campbell, L., Daneshfar, B., Filyer, P., Smith, A., Davidson, A., Shang, J., and Jarvis, I.: AAFC
846   annual crop inventory, 2013 Second International Conference on Agro-Geoinformatics (Agro-Geoinformatics), 270-
847   274,

848   Foody, G. M. and Arora, M. K.: An evaluation of some factors affecting the accuracy of classification by an artificial neural
849   network, Int. J. Remote Sens., 18, 799-810, https://doi.org/10.1080/014311697218764, 1997.

850   Fu, C., Cheng, L., Qin, S., Tariq, A., Liu, P., Zou, K., and Chang, L.: Timely plastic-mulched cropland extraction method from
851   complex mixed surfaces in arid regions, Remote Sens., 14, 4051, https://doi.org/10.3390/rs14164051, 2022.

852   Gao, H. H., Yan, C. R., Liu, Q., Ding, W. L., Chen, B. Q., and Li, Z.: Effects of plastic mulching and plastic residue on agricultural
853   production: A meta-analysis, Sci. Total Environ., 651, 484-492, https://doi.org/10.1016/j.scitotenv.2018.09.105, 2019.

854   Gao, Y., Pan, Y., Zhu, X., Li, L., Ren, S., Zhao, C., and Zheng, X.: FARM: A fully automated rice mapping framework combining
855   Sentinel-1 SAR and Sentinel-2 multi-temporal imagery, Comput. Electron. Agric., 213, 108262,
856   https://doi.org/10.1016/j.compag.2023.108262, 2023.

857   Gitelson, A. A., Viña, A., Ciganda, V., Rundquist, D. C., and Arkebauer, T. J.: Remote estimation of canopy chlorophyll content
858   in crops, Geophys. Res. Lett., 32, https://doi.org/10.1029/2005GL022688, 2005.

859   Gong, P., Liu, H., Zhang, M., Li, C., Wang, J., Huang, H., Clinton, N., Ji, L., Li, W., Bai, Y., Chen, B., Xu, B., Zhu, Z., Yuan, C.,
860   Ping Suen, H., Guo, J., Xu, N., Li, W., Zhao, Y., Yang, J., Yu, C., Wang, X., Fu, H., Yu, L., Dronova, I., Hui, F., Cheng,
861   X., Shi, X., Xiao, F., Liu, Q., and Song, L.: Stable classification with limited sample: transferring a 30-m resolution
862   sample set collected in 2015 to mapping 10-m resolution global land cover in 2017, Sci. Bull., 64, 370-373,
863   https://doi.org/10.1016/j.scib.2019.03.002, 2019.

864   Gorelick, N., Hancher, M., Dixon, M., Ilyushchenko, S., Thau, D., and Moore, R.: Google Earth Engine: Planetary-scale
865   geospatial analysis for everyone, Remote Sens. Environ., 202, 18-27, https://doi.org/10.1016/j.rse.2017.06.031, 2017.

866   Han, J., Zhang, Z., Luo, Y., Cao, J., Zhang, L., Zhang, J., and Li, Z.: The RapeseedMap10 database: annual maps of rapeseed at
867   a spatial resolution of 10 m based on multi-source data, Earth Syst. Sci. Data, 13, 2857-2874,
868   https://doi.org/10.5194/essd-13-2857-2021, 2021.

869   Hao, P., Di, L., Zhang, C., and Guo, L.: Transfer Learning for Crop classification with Cropland Data Layer data (CDL) as
870   training samples, Sci. Total Environ., 733, 138869, https://doi.org/10.1016/j.scitotenv.2020.138869, 2020.

871   Hao, P., Chen, Z., Tang, H., Li, D., and Li, H.: New workflow of plastic-mulched farmland mapping using multi-temporal
872   Sentinel-2 data, Remote Sens., 11, 1353, https://doi.org/10.3390/rs11111353, 2019.

873   Hasituya and Chen, Z.: Mapping plastic-mulched farmland with multi-temporal Landsat-8 data, Remote Sens., 9, 557,
874   https://doi.org/10.3390/rs9060557, 2017.

875   Hasituya, Chen, Z. X., Li, F., and Hu, Y. C.: Mapping plastic-mulched farmland by coupling optical and synthetic aperture radar
876   remote sensing, Int. J. Remote Sens., 41, 7757-7778, 2020.

877   Hasituya, Chen, Z., Wang, L., Wu, W., Jiang, Z., and Li, H.: Monitoring plastic-mulched farmland by Landsat-8 OLI imagery
878   using spectral and textural features, Remote Sens., 8, 353, https://doi.org/10.3390/rs8040353, 2016.

879   Hu, Y., Zeng, H., Tian, F., Zhang, M., Wu, B., Gilliams, S., Li, S., Li, Y., Lu, Y., and Yang, H.: An interannual transfer learning
880   approach for crop classification in the Hetao Irrigation District, China, Remote Sens., 14, 1208,
881   https://doi.org/10.3390/rs14051208, 2022.

882   Huang, H., Wang, J., Liu, C., Liang, L., Li, C., and Gong, P.: The migration of training samples towards dynamic global land
883   cover mapping, ISPRS J. Photogramm. Remote Sens., 161, 27-36, https://doi.org/10.1016/j.isprsjprs.2020.01.010, 2020.

884   Jakubauskas, M. E., Legates, D. R., and Kastens, J. H.: Harmonic analysis of time-series AVHRR NDVI data, Photogramm. Eng.
885   Remote Sens., 67, 461-470, 2001.

886   Kumar, M., Xiong, X., He, M., Tsang, D. C. W., Gupta, J., Khan, E., Harrad, S., Hou, D., Ok, Y. S., and Bolan, N. S.: Microplastics
887   as pollutants in agricultural soils, Environ. Pollut., 265, 114980, https://doi.org/10.1016/j.envpol.2020.114980, 2020.

888   Li, P., Li, H., Si, B., Zhou, T., Zhang, C., and Li, M.: Mapping planted forest age using LandTrendr algorithm and Landsat 5–8
889   on the Loess Plateau, China, Agric. For. Meteorol., 344, 109795, https://doi.org/10.1016/j.agrformet.2023.109795, 2024.

890   Li, Z., Zheng, F., Liu, W., and Jiang, D.: Spatially downscaling GCMs outputs to project changes in extreme precipitation and
891   temperature events on the Loess Plateau of China during the 21st Century, Glob. Planet. Change, 82-83, 65-73,
892   https://doi.org/10.1016/j.gloplacha.2011.11.008, 2012.

893   Liu, E. K., He, W. Q., and Yan, C. R.: 'White revolution'to 'white pollution'—agricultural plastic film mulch in China, Environ.
894   Res. Lett., 9, 091001, https://doi.org/10.1088/1748-9326/9/9/091001, 2014.

895   Liu, H., Gong, P., Wang, J., Clinton, N., Bai, Y., and Liang, S.: Annual dynamics of global land cover and its long-term changes
896   from 1982 to 2015, Earth Syst. Sci. Data, 12, 1217-1243, 2020.

897   Liu, W. and Zhang, H.: Mapping annual 10 m rapeseed extent using multisource data in the Yangtze River Economic Belt of
898   China (2017–2021) on Google Earth Engine, Int. J. Appl. Earth Obs. Geoinf., 117, 103198,
899   https://doi.org/10.1016/j.jag.2023.103198, 2023.

900   Lu, L., Hang, D., and Di, L.: Threshold model for detecting transparent plastic-mulched landcover using moderate-resolution
901   imaging spectroradiometer time series data: a case study in southern Xinjiang, China, J. Appl. Remote Sens., 9, 097094,
902   https://doi.org/10.1117/1.JRS.9.097094, 2015.

903   Lu, L., Tao, Y., and Di, L.: Object-based plastic-mulched landcover extraction using integrated Sentinel-1 and Sentinel-2 data,
904   Remote Sens., 10, 1820, https://doi.org/10.3390/rs10111820, 2018.

905   Lu, L. Z., Di, L. P., and Ye, Y. M.: A decision-tree classifier for extracting transparent plastic-mulched landcover from Landsat-
906   5 TM images, IEEE J. Sel. Top. Appl. Earth Observ. Remote Sens., 7, 4548-4558,
907   https://doi.org/10.1109/JSTARS.2014.2327226, 2014.

908   Luo, Y., Zhang, Z., Zhang, L., Han, J., Cao, J., and Zhang, J.: Developing high-resolution crop maps for major crops in the
909   European Union based on transductive transfer learning and limited ground data, Remote Sens., 14, 1809,
910   https://doi.org/10.3390/rs14081809, 2022.

911   Ma, Y., Chen, S., Ermon, S., and Lobell, D. B.: Transfer learning in environmental remote sensing, Remote Sens. Environ., 301,
912   113924, https://doi.org/10.1016/j.rse.2023.113924, 2024.

913   Maselli, F., Battista, P., Chiesi, M., Rapi, B., Angeli, L., Fibbi, L., Magno, R., and Gozzini, B.: Use of Sentinel-2 MSI data to
914   monitor crop irrigation in Mediterranean areas, Int. J. Appl. Earth Obs. Geoinf., 93, 102216,
915   https://doi.org/10.1016/j.jag.2020.102216, 2020.

916   Orynbaikyzy, A., Gessner, U., and Conrad, C.: Spatial transferability of random forest models for crop type classification using
917   Sentinel-1 and Sentinel-2, Remote Sens., 14, 1493, https://doi.org/10.3390/rs14061493, 2022.

918   Pan, S. J. and Yang, Q.: A survey on transfer learning, IEEE Trans. Knowl. Data Eng., 22, 1345-1359,

919   https://doi.org/10.1109/TKDE.2009.191, 2009.

920 Pham-Duc, B., Nguyen, H., Phan, H., and Tran-Anh, Q.: Trends and applications of google earth engine in remote sensing and
921   earth science research: A bibliometric analysis using scopus database, Earth Sci. Inform., 16, 2355-2371,
922   https://doi.org/10.1007/s12145-023-01035-2, 2023.

923 Phiri, D., Simwanda, M., Salekin, S., Nyirenda, V. R., Murayama, Y., and Ranagalage, M.: Sentinel-2 data for land cover/use
924   mapping: A review, Remote Sens., 12, 2291, https://doi.org/10.3390/rs12142291, 2020.

925 Qadir, A., Skakun, S., Becker-Reshef, I., Kussul, N., and Shelestov, A.: Estimation of sunflower planted areas in Ukraine during
926   full-scale Russian invasion: Insights from Sentinel-1 SAR data, Science of Remote Sensing, 10, 100139,
927   https://doi.org/10.1016/j.srs.2024.100139, 2024a.

928 Qadir, A., Skakun, S., Kussul, N., Shelestov, A., and Becker-Reshef, I.: A generalized model for mapping sunflower areas using
929   Sentinel-1 SAR data, Remote Sens. Environ., 306, 114132, https://doi.org/10.1016/j.rse.2024.114132, 2024b.

930 Rasul, A., Balzter, H., Ibrahim, G. R. F., Hameed, H. M., Wheeler, J., Adamu, B., Ibrahim, S. a., and Najmaddin, P. M.: Applying
931   built-up and bare-soil indices from Landsat 8 to cities in dry climates, Land, 7, 81, https://doi.org/10.3390/land7030081,
932   2018.

933 Rikimaru, A., Roy, P. S., and Miyatake, S.: Tropical forest cover density mapping, Trop. Ecol., 43, 39-47, 2002.

934 Sheykhmousa, M., Mahdianpari, M., Ghanbari, H., Mohammadimanesh, F., Ghamisi, P., and Homayouni, S.: Support vector
935   machine versus random forest for remote sensing image classification: A meta-analysis and systematic review, IEEE J.
936   Sel. Top. Appl. Earth Observ. Remote Sens., 13, 6308-6325, https://doi.org/10.1109/JSTARS.2020.3026724, 2020.

937 Skakun, S., Franch, B., Vermote, E., Roger, J. C., Becker-Reshef, I., Justice, C., and Kussul, N.: Early season large-area winter
938   crop mapping using MODIS NDVI data, growing degree days information and a Gaussian mixture model, Remote Sens.
939   Environ., 195, 244-258, https://doi.org/10.1016/j.rse.2017.04.026, 2017.

940 Song, X., Potapov, P. V., Krylov, A., King, L., Bella, C. M. D., Hudson, A., Khan, A., Adusei, B., Stehman, S. V., and Hansen,
941   M. C.: National-scale soybean mapping and area estimation in the United States using medium resolution satellite
942   imagery and field survey, Remote Sens. Environ., 190, 383-395, https://doi.org/10.1016/j.rse.2017.01.008, 2017.

943 Sun, D., Li, H., Wang, E., He, W., Hao, W., Yan, C., Li, Y., Mei, X., Zhang, Y., and Sun, Z.: An overview of the use of plastic-
944   film mulching in China to increase crop yield and water-use efficiency, Natl. Sci. Rev., 7, 1523-1526,
945   https://doi.org/10.1093/nsr/nwaa146, 2020.

946 Tamiminia, H., Salehi, B., Mahdianpari, M., Quackenbush, L., Adeli, S., and Brisco, B.: Google Earth Engine for geo-big data
947   applications: A meta-analysis and systematic review, ISPRS J. Photogramm. Remote Sens., 164, 152-170,
948   https://doi.org/10.1016/j.isprsjprs.2020.04.001, 2020.

949 Tang, X., Miao, C., Xi, Y., Duan, Q., Lei, X., and Li, H.: Analysis of precipitation characteristics on the loess plateau between
950   1965 and 2014, based on high-density gauge observations, Atmos. Res., 213, 264-274,
951   https://doi.org/10.1016/j.atmosres.2018.06.013, 2018.

952 Tong, X., Zhang, X., Fensholt, R., Jensen, P. R. D., Li, S., Larsen, M. N., Reiner, F., Tian, F., and Brandt, M.: Global area boom
953   for greenhouse cultivation revealed by satellite mapping, Nat. Food, 5, 513-523, https://doi.org/10.1038/s43016-024-
954   00985-0, 2024.

955 Tu, Y., Wu, S., Chen, B., Weng, Q., Bai, Y., Yang, J., Yu, L., and Xu, B.: A 30 m annual cropland dataset of China from 1986 to
956   2021, Earth Syst. Sci. Data, 16, 2297-2316, https://doi.org/10.5194/essd-16-2297-2024, 2024.

957 Tucker, C. J.: Red and photographic infrared linear combinations for monitoring vegetation, Remote Sens. Environ., 8, 127-150,
958   https://doi.org/10.1016/0034-4257(79)90013-0, 1979.

959 Veettil, B. K., Van, D. D., Quang, N. X., and Hoai, P. N.: Remote sensing of plastic-covered greenhouses and plastic-mulched
960   farmlands: Current trends and future perspectives, Land Degrad. Dev., 34, 591-609, https://doi.org/10.1002/ldr.4497,
961   2023.

962 Wang, J., Xie, J., Li, L., and Adingo, S.: Review on the fully mulched ridge–furrow system for sustainable maize production on
963   the semi-arid Loess Plateau, J. Integr. Agric., 22, 1277-1290, https://doi.org/10.1016/j.jia.2022.09.023, 2023.

964 Wang, L. and Qu, J. J.: NMDI: A normalized multi-band drought index for monitoring soil and vegetation moisture with satellite

965   remote sensing, Geophys. Res. Lett., 34, https://doi.org/10.1029/2007GL031021, 2007.

966   Wang, P., Fan, E., and Wang, P.: Comparative analysis of image classification algorithms based on traditional machine learning

967   and deep learning, Pattern Recognit. Lett., 141, 61-67, https://doi.org/10.1016/j.patrec.2020.07.042, 2021.

968   Wang, S., Azzari, G., and Lobell, D. B.: Crop type mapping without field-level labels: Random forest transfer and unsupervised

969   clustering techniques, Remote Sens. Environ., 222, 303-317, https://doi.org/10.1016/j.rse.2018.12.026, 2019.

970   Wang, S., Di Tommaso, S., Deines, J. M., and Lobell, D. B.: Mapping twenty years of corn and soybean across the US Midwest

971   using the Landsat archive, Sci. Data, 7, 307, 2020.

972   Wang, S., Fan, T., Cheng, W., Wang, L., Zhao, G., Li, S., Dang, Y., and Zhang, J.: Occurrence of macroplastic debris in the long-

973   term plastic film-mulched agricultural soil: A case study of Northwest China, Sci. Total Environ., 831, 154881,

974   https://doi.org/10.1016/j.scitotenv.2022.154881, 2022a.

975   Wang, S., Feng, W., Quan, Y., Li, Q., Dauphin, G., Huang, W., Li, J., and Xing, M.: A heterogeneous double ensemble algorithm

976   for soybean planting area extraction in Google Earth Engine, Comput. Electron. Agric., 197, 106955,

977   https://doi.org/10.1016/j.compag.2022.106955, 2022b.

978   Wang, Y. P., Li, X. G., Zhu, J., Fan, C. Y., Kong, X. J., Turner, N. C., Siddique, K. H. M., and Li, F.-M.: Multi-site assessment of

979   the effects of plastic-film mulch on dryland maize productivity in semiarid areas in China, Agric. For. Meteorol., 220,

980   160-169, https://doi.org/10.1016/j.agrformet.2016.01.142, 2016.

981   Weiss, M., Jacob, F., and Duveiller, G.: Remote sensing for agricultural applications: A meta-review, Remote Sens. Environ.,

982   236, 111402, https://doi.org/10.1016/j.rse.2019.111402, 2020.

983   Wen, Y., Li, X., Mu, H., Zhong, L., Chen, H., Zeng, Y., Miao, S., Su, W., Gong, P., Li, B., and Huang, J.: Mapping corn dynamics

984   using limited but representative samples with adaptive strategies, ISPRS J. Photogramm. Remote Sens., 190, 252-266,

985   https://doi.org/10.1016/j.isprsjprs.2022.06.012, 2022.

986   Wijesingha, J., Dzene, I., and Wachendorf, M.: Evaluating the spatial–temporal transferability of models for agricultural land

987   cover mapping using Landsat archive, ISPRS J. Photogramm. Remote Sens., 213, 72-86,

988   https://doi.org/10.1016/j.isprsjprs.2024.05.020, 2024.

989   Xiao, X., Boles, S., Liu, J., Zhuang, D., and Liu, M.: Characterization of forest types in Northeastern China, using multi-temporal

990   SPOT-4 VEGETATION sensor data, Remote Sens. Environ., 82, 335-348, https://doi.org/10.1016/S0034-

991   4257(02)00051-2, 2002.

992   Xiong, Y., Zhang, Q., Chen, X., Bao, A., Zhang, J., and Wang, Y.: Large scale agricultural plastic mulch detecting and monitoring

993   with multi-source remote sensing data: A case study in Xinjiang, China, Remote Sens., 11, 2088,

994   https://doi.org/10.3390/rs11182088, 2019.

995   Xu, J., Yang, J., Xiong, X., Li, H., Huang, J., Ting, K. C., Ying, Y., and Lin, T.: Towards interpreting multi-temporal deep learning

996   models in crop mapping, Remote Sens. Environ., 264, 112599, https://doi.org/10.1016/j.rse.2021.112599, 2021.

997   Xuan, F., Dong, Y., Li, J., Li, X., Su, W., Huang, X., Huang, J., Xie, Z., Li, Z., Liu, H., Tao, W., Wen, Y., and Zhang, Y.: Mapping

998   crop type in Northeast China during 2013–2021 using automatic sampling and tile-based image classification, Int. J.

999   Appl. Earth Obs. Geoinf., 117, 103178, https://doi.org/10.1016/j.jag.2022.103178, 2023.

1000   Yan, C., Liu, E., Shu, F., Liu, Q., Liu, S., and He, W.: Review of agricultural plastic mulching and its residual pollution and

1001   prevention measures in China (in Chinese), Journal of Agricultural Resources and Environment, 31, 95-102,

1002   https://doi.org/10.13254/j.jare.2013.0223, 2014.

1003   Yang, G., Li, X., Liu, P., Yao, X., Zhu, Y., Cao, W., and Cheng, T.: Automated in-season mapping of winter wheat in China with

1004   training data generation and model transfer, ISPRS J. Photogramm. Remote Sens., 202, 422-438,

1005   https://doi.org/10.1016/j.isprsjprs.2023.07.004, 2023.

1006   Yang, J. and Huang, X.: The 30 m annual land cover dataset and its dynamics in China from 1990 to 2019, Earth Syst. Sci. Data,

1007   13, 3907-3925, https://doi.org/10.5194/essd-13-3907-2021, 2021.

1008   Yang, N., Liu, D., Feng, Q., Xiong, Q., Zhang, L., Ren, T., Zhao, Y., Zhu, D., and Huang, J.: Large-scale crop mapping based on

1009   machine learning and parallel computation with grids, Remote Sens., 11, 1500, https://doi.org/10.3390/rs11121500,

1010   2019.

1011 Yang, N., Sun, Z., Feng, L., Zheng, M., Chi, D., Meng, W., Hou, Z., Bai, W., and Li, K.: Plastic film mulching for water-efficient
1012   agricultural applications and degradable films materials development research, Mater. Manuf. Process., 30, 143-154,
1013   https://doi.org/10.1080/10426914.2014.930958, 2015.

1014 You, N. and Dong, J.: Examining earliest identifiable timing of crops using all available Sentinel 1/2 imagery and Google Earth
1015   Engine, ISPRS J. Photogramm. Remote Sens., 161, 109-123, https://doi.org/10.1016/j.isprsjprs.2020.01.001, 2020.

1016 You, N., Dong, J., Li, J., Huang, J., and Jin, Z.: Rapid early-season maize mapping without crop labels, Remote Sens. Environ.,
1017   290, 113496, https://doi.org/10.1016/j.rse.2023.113496, 2023.

1018 You, N., Dong, J., Huang, J., Du, G., Zhang, G., He, Y., Yang, T., Di, Y., and Xiao, X.: The 10-m crop type maps in Northeast
1019   China during 2017–2019, Sci. Data, 8, 41, https://doi.org/10.1038/s41597-021-00827-9, 2021.

1020 Zanaga, D., Van De Kerchove, R., Daems, D., De Keersmaecker, W., Brockmann, C., Kirches, G., Wevers, J., Cartus, O., Santoro,
1021   M., and Fritz, S.: ESA WorldCover 10 m 2021 v200, https://doi.org/10.5281/zenodo.5571936, 2022.

1022 Zang, Y., Qiu, Y., Chen, X., Chen, J., Yang, W., Liu, Y., Peng, L., Shen, M., and Cao, X.: Mapping rapeseed in China during
1023   2017-2021 using Sentinel data: an automated approach integrating rule-based sample generation and a one-class
1024   classifier (RSG-OC), GISci. Remote Sens., 60, 2163576, https://doi.org/10.1080/15481603.2022.2163576, 2023.

1025 Zhang, C., Dong, J., and Ge, Q.: IrriMap_CN: Annual irrigation maps across China in 2000–2019 based on satellite observations,
1026   environmental variables, and machine learning, Remote Sens. Environ., 280, 113184,
1027   https://doi.org/10.1016/j.rse.2022.113184, 2022a.

1028 Zhang, C., Zhang, H., and Tian, S.: Phenology-assisted supervised paddy rice mapping with the Landsat imagery on Google
1029   Earth Engine: Experiments in Heilongjiang Province of China from 1990 to 2020, Comput. Electron. Agric., 212,
1030   108105, https://doi.org/10.1016/j.compag.2023.108105, 2023.

1031 Zhang, C., Zhang, H., and Zhang, L.: Spatial domain bridge transfer: An automated paddy rice mapping method with no training
1032   data required and decreased image inputs for the large cloudy area, Comput. Electron. Agric., 181, 105978,
1033   https://doi.org/10.1016/j.compag.2020.105978, 2021a.

1034 Zhang, C., Dong, J., Xie, Y., Zhang, X., and Ge, Q.: Mapping irrigated croplands in China using a synergetic training sample
1035   generating method, machine learning classifier, and Google Earth Engine, Int. J. Appl. Earth Obs. Geoinf., 112, 102888,
1036   https://doi.org/10.1016/j.jag.2022.102888, 2022b.

1037 Zhang, D., Pan, Y., Zhang, J., Hu, T., Zhao, J., Li, N., and Chen, Q.: A generalized approach based on convolutional neural
1038   networks for large area cropland mapping at very high resolution, Remote Sens. Environ., 247, 111912,
1039   https://doi.org/10.1016/j.rse.2020.111912, 2020a.

1040 Zhang, H., Liu, W., and Zhang, L.: Seamless and automated rapeseed mapping for large cloudy regions using time-series optical
1041   satellite imagery, ISPRS J. Photogramm. Remote Sens., 184, 45-62, https://doi.org/10.1016/j.isprsjprs.2021.12.001,
1042   2022c.

1043 Zhang, H., Wang, Y., Shang, J., Liu, M., and Li, Q.: Investigating the impact of classification features and classifiers on crop
1044   mapping performance in heterogeneous agricultural landscapes, Int. J. Appl. Earth Obs. Geoinf., 102, 102388,
1045   https://doi.org/10.1016/j.jag.2021.102388, 2021b.

1046 Zhang, H. K. and Roy, D. P.: Using the 500 m MODIS land cover product to derive a consistent continental scale 30 m Landsat
1047   land cover classification, Remote Sens. Environ., 197, 15-34, https://doi.org/10.1016/j.rse.2017.05.024, 2017.

1048 Zhang, H. Y., Kang, J. Z., Xu, X., and Zhang, L. P.: Accessing the temporal and specral features in crop type mapping using
1049   multi-temporal Sentinel-2 imagery: A case study of Yi'an Country, Heilongjiang province, China, Comput. Electron.
1050   Agric., 176, 105618, https://doi.org/10.1016/j.compag.2020.105618, 2020b.

1051 Zhang, J., Ren, S., Dai, J., Ding, F., Xiao, M., Liu, X., Yan, C., Ge, T., Wang, J., Liu, Q., Wang, K., and Zhang, F.: Influence of
1052   plastic film on agricultural production and its pollution control (in Chinese), Scientia Agricultura Sinica, 55, 3983-3996,
1053   https://doi.org/10.3864/j.issn.0578-1752.2022.20.010, 2022d.

1054 Zhang, L., Zhang, K., Zhu, X., Chen, H., and Wang, W.: Integrating remote sensing, irrigation suitability and statistical data for
1055   irrigated cropland mapping over mainland China, J. Hydrol., 613, 128413,
1056   https://doi.org/10.1016/j.jhydrol.2022.128413, 2022e.

1057   Zhang, L., Wang, W., Ma, Q., Hu, Y., Ma, H., and Zhao, Y.: CCropLand30: High-resolution hybrid cropland maps of China
1058   created through the synergy of state-of-the-art remote sensing products and the latest national land survey, Comput.
1059   Electron. Agric., 218, 108672, https://doi.org/10.1016/j.compag.2024.108672, 2024.

1060   Zhang, L., Qin, R., Wei, H., Zhang, K., Yu, C., Li, F., and Zhang, F.: Optimum plastic mulching application to reduce greenhouse
1061   gas emissions without compromising on crop yield and farmers' income, Sci. Total Environ., 809, 151998,
1062   https://doi.org/10.1016/j.scitotenv.2021.151998, 2022f.

1063   Zhang, P., Du, P., Guo, S., Zhang, W., Tang, P., Chen, J., and Zheng, H.: A novel index for robust and large-scale mapping of
1064   plastic   greenhouse   from   Sentinel-2   images,   Remote   Sens.   Environ.,   276,   113042,
1065   https://doi.org/10.1016/j.rse.2022.113042, 2022g.

1066   Zhang, X., Liu, L., Chen, X., Gao, Y., Xie, S., and Mi, J.: GLC_FCS30: Global land-cover product with fine classification system
1067   at 30 m using time-series Landsat imagery, Earth Syst. Sci. Data, 13, 2753-2776, https://doi.org/10.5194/essd-13-2753-
1068   2021, 2021c.

1069   Zhao, C., Luo, Y., Chen, X., Wu, L., Wang, Z., Feng, H., Yu, Q., and He, J.: PMF-LP: the first 10 m plastic-mulched farmland
1070   distribution map (2019-2021) in the Loess Plateau of China generated using training sample generation and classifier
1071   transfer method, Zenodo [data set], https://doi.org/10.5281/zenodo.13369426, 2024.

1072   Zhao, Y., Mao, X., Li, S., Huang, X., Che, J., and Ma, C.: A review of plastic film mulching on water, heat, nitrogen balance,
1073   and crop growth in farmland in China, Agronomy-Basel, 13, 2515, https://doi.org/10.3390/agronomy13102515, 2023.

1074   Zheng, W., Wang, R., Cao, Y., Jin, N., Feng, H., and He, J.: Remote sensing recognition of plastic-film-mulched farmlands on
1075   Loess Plateau based on Google Earth Engine (in Chinese), Transactions of the Chinese Society for Agricultural
1076   Machinery, 53, 224-234, https://doi.org/10.6041/j.issn.1000-1298.2022.01.025, 2022.

1077   Zhong, L., Hu, L., and Zhou, H.: Deep learning based multi-temporal crop classification, Remote Sens. Environ., 221, 430-443,
1078   https://doi.org/10.1016/j.rse.2018.11.032, 2019.

1079   Zhou, C., Huang, J., Xiao, Y., Du, M., and Li, S.: A novel approach: Coupling prior knowledge and deep learning methods for
1080   large-scale plastic greenhouse extraction using Sentinel-1/2 data, Int. J. Appl. Earth Obs. Geoinf., 132, 104073,
1081   https://doi.org/10.1016/j.jag.2024.104073, 2024.

1082   Zhou, Q., Zhu, Z., Xian, G., and Li, C.: A novel regression method for harmonic analysis of time series, ISPRS J. Photogramm.
1083   Remote Sens., 185, 48-61, https://doi.org/10.1016/j.isprsjprs.2022.01.006, 2022.

1084   Zhou, W., Wei, H., Chen, Y., Zhang, X., Hu, J., Cai, Z., Yang, J., Hu, Q., Xiong, H., Yin, G., and Xu, B.: Monitoring intra-annual
1085   and interannual variability in spatial distribution of plastic-mulched citrus in cloudy and rainy areas using multisource
1086   remote sensing data, Eur. J. Agron., 151, 126981, https://doi.org/10.1016/j.eja.2023.126981, 2023.

1087   Zou, Q., Ni, L., Zhang, T., and Wang, Q.: Deep learning based feature selection for remote sensing scene classification, IEEE
1088   Geosci. Remote Sens. Lett., 12, 2321-2325, https://doi.org/10.1109/LGRS.2015.2475299, 2015.

1089